What controls lateral segmentation in Cascadia? Sub-slab density anomalies or slab age variations?

Sassard, V.L. (Vince) - 8837815

Utrecht University
MSc Thesis 2021 -2022
1st supervisor: Dr. Ylona van Dinther (Utrecht University)
2nd supervisor: Dr. Miles Bodmer (Sandia National Laboratories)

Abstract

The Cascadia Subduction Zone (CSZ) reveals along-strike segmentation of the subduction zone into three regions. Variations in topography, slab dip, interseimsic coupling, and seismicity in two segments (Northern and Southern Cascadia) have been described but the explanation of this segmentation remains unclear. It has been proposed that they result from the presence of low-density anomalies beneath the slab (Bodmer et al., 2018) and variations in incoming slab age. Here, I evaluate both hypotheses using a physics-based numerical model allowing to follow both long- and short-term changes of a subduction zone. Here, I show that sub-slab buoyancy tends to make the slab dip steeper at the seismogenic zone but shallower at geodynamics depths. The shallowing of the slab at geodynamic depths produces an upward push onto the overriding plate that forms highs in topography. Some of this upward force is being absorbed by the elasticity of the plate and the non-elastic behavior of the lower crust of the continent. In the shorter timescale, with an increasing density contrast, the interseismic coupling decreases in the updip region in favor of creep at the interface while in the downdip region, it decreases by increasing the viscosity at the interface. The seismicity is more frequent, and ruptures occur along narrower widths because the steeper slab dip and the increased slab curvature limit their propagation by increasing the amount of heterogeneities. On the other hand, the younger a plate is, the steeper its slab dip is at the seismogenic zone due to its low resistivity to bending. Nevertheless, their buoyancy makes them push more against the overrding plate before sining resulting in higher topography. The interface between the oceanic slab and the overriding plate tends is warmer the younger a plate is leading to lower viscosities and, therefore, lower coupling, and narrower seismogenic zone, so lower ruptures. Finally, based on a minor extrapolation I show that density contrasts alone can explain the variations in topography, seismicity, and coupling in the downdip region. This demonstrates that mantle dynamic features do not only have a real and lasting impact on topography, but also on seismic hazard in subduction zones which release most of the seismic moment on our planet.

Table of Contents

1. Introduction

Subduction zones are locations where key processes for plate tectonics take place, which result in the recycling of the oceanic lithosphere into the mantle as well as production of new continental material. Megathrust earthquakes are major earthquakes happening at the interface between the subducting slab and the overriding plate. Megathrust earthquakes produce most of the seismic moments on our planet which makes subduction zones highly hazardous for surrounding populations. Subduction dynamics have been extensively studied for the past 40 years (e.g., Long and Silver (2009); Schellart and Rawlinson (2010); Long (2013); Wirth and Long (2013); Bodmer et al. (2020), Delph et al. (2021)) as well as the interplays between the different elements of subduction zones such as mantle flow on the forearc topography (Braun, 2010). In the meantime, numerical modeling has also greatly developed and has significantly contributed to the better understanding of subduction zones at all time scales (Jadamec and Billen (2010); Faccenda and Capitanio (2013); van Dinther et al. (2009; 2013a); Brizzi et al. (2018)). Nevertheless, some processes remain poorly understood, especially in the sub-slab region. The relations between mantle dynamics and seismicity along the interface between the two plates are also relatively unclear. It has been proposed that the subduction dynamics can be affected by both the morphology of the slab and the adjacent mantle flow (e.g., Jadamec and Billen, 2010; Paczkowski et al., 2014; Bodmer et al., 2018; 2020, Venereau et al., 2018). The morphology of the slab has been suggested to be influenced by the age of the plate (Kelsey et al. (1994)) and sub-slab characteristics (Bodmer et al. (2018; 2020); Betts et al. (2012); Honda et al. (2007)). To study the effects of plate age versus sub-slab characteristics, the Cascadia Subduction Zone (CSZ) is an ideal location because of its along-strike heterogeneity in seismicity, morphology of the slab, the overriding plate, and its sub-slab region (Figure 1).

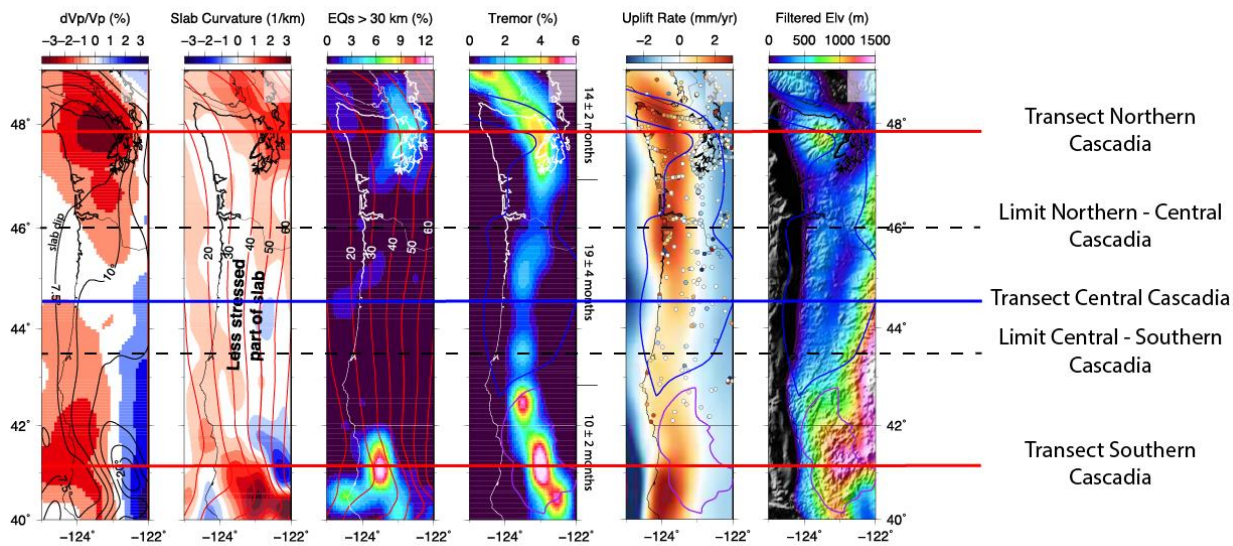

Figure 1: Geophysical data in Cascadia (modified from Delph et al., 2021) overlaid by the three transects presented in this study. The blue line represents the Central Cascadia transect and the red lines represent the Northern and Southern Cascadia transects supposedly affected by the sub-slab buoyant anomalies (Bodmer et al., 2018; 2020). The black dashed lines indicate the limits of the segments Northern, Central, and Southern Cascadia. The blue contours represent the Siletzia terrane.

With the deployment of the Cascadia Initiative (Toomey et al., 2014), an onshore offshore seismic experiment, studies have been able to capture more details of this subduction zone and propose geodynamic models to explain their new observations. Bodmer et al. (2018; 2020), using a seismic tomography model, described variations in seismic velocities below the slab that they interpreted as corresponding to a density contrast induced by independent mantle upwellings in Northern and Southern Cascadia (Figure 2). The sub-slab low velocity anomalies correlate with a ~2-degree shallower slab dip (McCrory et al., 2012), ~1,000-meter higher

forearc topography (Bodmer et al. (2018; 2020)), ~0.3 higher locking fraction (Schmalzle et al. 2014), ~2-mm/yr increased uplift rates (Schmalzle et al. 2014), and 3-4 times higher density of large earthquakes and tremors (Bodmer et al., 2018; 2020; Delph et al., 2021) (Figures 2 & 3). Bodmer et al. (2018; 2020)'s studies challenge the previous conceptual model proposed by Kelsey et al. (1994) where the variations of slab age along-strike (7.5 – 18.8 Ma) are the main driver of the heterogeneities observed in slab dip, topography, and seismicity. Wilson (2002) introduced a alternative plate age model for Cascadia where the age variations are narrower (9 – 13 Ma, ~4 Ma instead of ~11 Ma), and are believed to be more appropriate for Cascadia and not sufficient to explain the along-strike variations (Bodmer et al. (2018; 2020); Delph et al. (2021); Fan and Zhao (2021)).

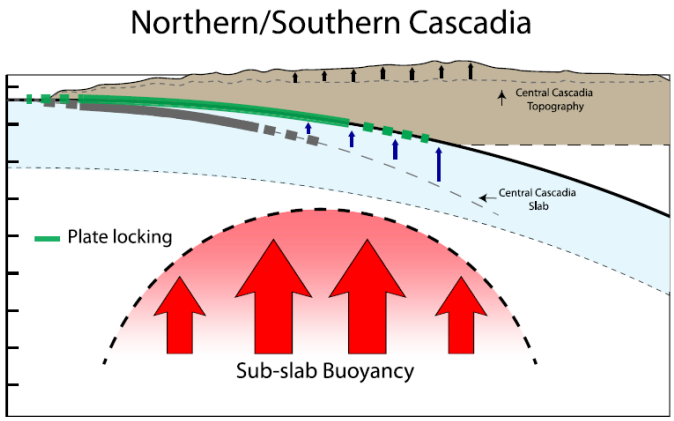

Figure 2: Conceptual model of subslab buoyancy's on Cascadia proposed by Bodmer et al. (2018; 2020)). The dashed gray lines correspond to the morphology of the plates interacting in Central Cascadia while the green and black continuous lines correspond to the situation in Northern and Southern Cascadia affected by the sub-slab buoyancy in red here.

The seismic observations in the sub-slab region along with the topography, slab dip, locking fraction, and seismicity led previous studies to divide the subduction zone into three distinct segments (Porritt et al. (2011); Chen et al. (2015); Krueger and Wirth (2017); Bodmer et al. (2018; 2020); Delph et al. (2021)) (Figure 1), two of which are suggested to be influenced by the upward push of the sub-slab buoyant anomalies, i.e., Northern and Southern Cascadia (Bodmer et al., 2018; 2020). Zhao and Hua (2021) use anisotropic tomography to support the hypothesis of Bodmer et al. (2018; 2020) where the Cobb hotspot affects the morphology and seismicity of the subduction zone but, in Southern Cascadia, they do not find any evidence for the presence of mantle upwelling. Fan and Zhao (2021) explain the along-strike variations in morphology, locking fraction, and seismicity by introducing two mechanical processes: the subduction slab morphology increases shear stress at the interface, so stress accumulates until a megathrust earthquake is triggered, or a high heat flux exist in these regions that changes the rheology at the interface from frictional to viscous. Delph et al. (2021) suggest that the morphology of the margin and its seismicity can be explained by "subcretion", i.e., the subduction of sediments.

Other studies have investigated the effect of a hotspot on a subduction zone through numerical modeling and found that a plume head can have very strong effects on subduction dynamics such as slab tear in the case of a retreating trench (Betts et al., 2012) or that it can remain at the same place for several dozens of million years and, therefore, interact with the slab over long periods (Honda et al. (2007)).

In this MSc thesis, I test the conceptual model derived by (Bodmer et al. (2018; 2020)) from the referenced tomographic models (Porritt et al. (2011); Bodmer et al., 2018; 2020; Delph et al. (2021), Zhao and Hua (2021)) through numerical modeling using the seismo-thermo-mechanical (STM) code developed by van Dinther et al. (2013). This physics-based code allows study of both the long-term evolution of the subduction zone (morphology, geometry) as well as transient events (seismicity). To do this, I study the impact of a sub-slab

buoyant anomaly and plate age on the subduction morphology, interseismic coupling, and seismicity, and compare them to understand how parameter may drive of the segmentation of the CSZ. I also discuss the relations between the sub-slab buoyancy characteristics derived from the model and the observations. This is addressed by comparing the modeling predictions to the observations of slab dip, elevation, interseismic coupling, magnitudes of the earthquakes.

1.1. Tectonic setting

The Cascadia Subduction Zone (CSZ) lies along the Northwestern American Coast where the Explorer, Juan de Fuca, and Gorda plates (i.e., Juan de Fuca system) subduct beneath the North American plate in a northeastward direction at a velocity of 40 mm/yr (DeMets et al., 2010). These three plates are the remnants of the larger Farallon plate which has been subducting under North America for, at least, the past 100 Ma (Schmid et al., 2002). Cascadia is a particularly narrow and young subduction zone with respect to the others which makes it a warm and, potentially, weak slab (Long, 2016). As a matter of fact, the subducting plate is about 9 ± 2 Ma at the trench (Wilson, 2002) and extends over 1,400 km from Washington down to Northern California. Despite its limited extent, Cascadia is relatively heterogeneous. Based on topography, slab morphology, seismicity, and geodesy, previous studies have divided it into three broad segments: Southern, Central, and Northern Cascadia (Porritt et al. (2011); Long (2016); Bodmer et al., 2018; 2020; Delph (2021)) (Figure 1).

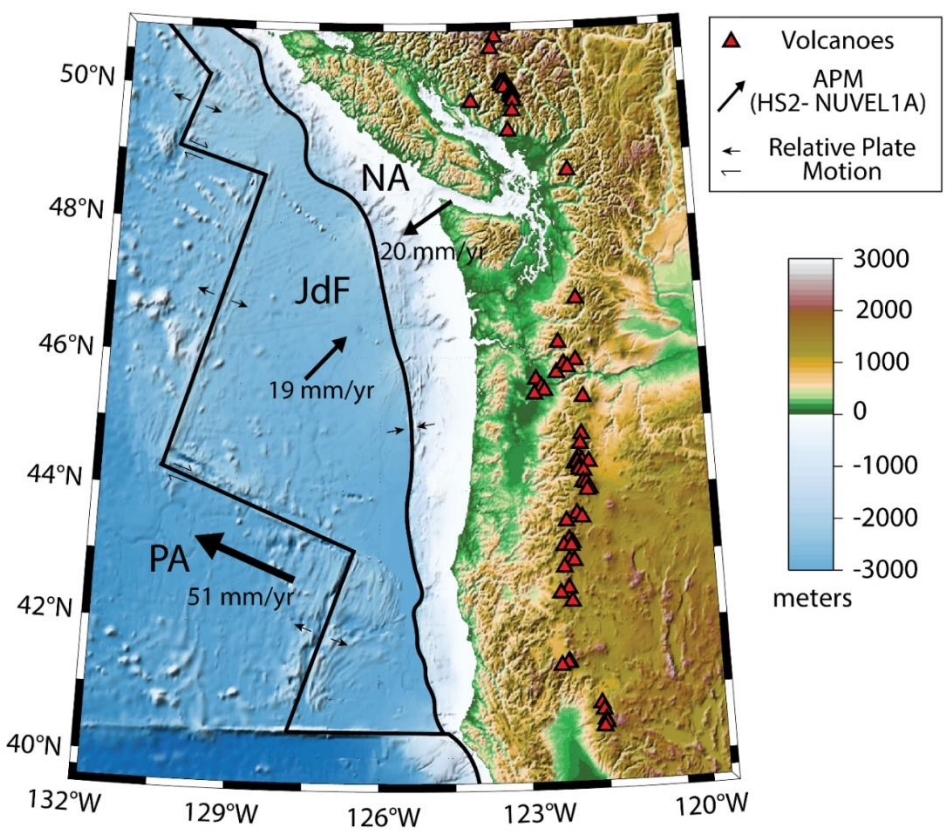

Figure 3: Tectonic map of the Cascadia subduction zone. PA, JdF, and NA represent the tectonic plates in the region with PA = Pacific, JdF = Juan de Fuca, and NA = North America. The large arrows associated with a velocity are the absolute plate motions of the plates (calculated with the UNAVCO plate motion calculator using the HS2-NUVEL1A model, DeMets et al., 2010). The smaller arrows on either side of the plate boundaries (black solid lines) are the relative plate motion for convergence, divergence, and transform motions. The colormap represents the elevation. The red and black triangles show the volcanoes (Cascades).

2. Methods

2.1. Numerical method

I use the seismo-thermo-mechanical (STM) code developed by van Dinther et al. (2013a, b; 2014) based on the classical geodynamic code I2ELVIS (Gerya and Yuen, 2007). The STM code is a 2-D code that relies on a Lagrangian marker-in-cell technique which implies that the displacement of a particle is followed in a referential that is the cell. The location of the markers as well as the physics variables (e.g., pressure, stress, strain…) at these markers is monitored through time and space. The markers are located on an undeformable Eulerian grid. The code utilizes an implicit 2-dimensional Finite Difference scheme to solve for the continuity equation (i.e., conservation of mass (1)) assuming an incompressible medium, the equation of motion (i.e., conservation of momentum), and the energy equation ((4)-(7)):

$$\frac{\partial v_x}{\partial x} + \frac{\partial v_z}{\partial z} = 0 \tag{1}$$

$$\frac{\partial \sigma'_{xx}}{\partial x} + \frac{\partial \sigma'_{xz}}{\partial z} - \frac{\partial P}{\partial z} = \rho \frac{Dv_x}{Dt} \tag{2}$$

$$\frac{\partial \sigma'_{zx}}{\partial x} + \frac{\partial \sigma'_{zz}}{\partial z} - \frac{\partial P}{\partial z} = \rho \frac{Dv_z}{Dt} - \rho g \tag{3}$$

Where, v_x and v_z are the horizontal and vertical velocities, respectively. σ'_{xx} and σ'_{xz} are the normal and shear components of the deviatoric stress tensor. P is the pressure. $\rho \frac{Dv_z}{Dt}$ is the inertial term where ρ is the density and $\frac{Dv_z}{Dt}$ is the Lagrangian time derivative of velocity. The inertial term stabilizes high slip rates when using small time steps. g is the gravity acceleration (g = 9.81 m/s^2).

I work in a Lagrangian framework, to follow the evolution of temperature through time, I need to solve for the energy equation using its Lagrangian form:

$$\rho C_p \left(\frac{DT}{Dt}\right) = -\frac{\partial q_x}{\partial x} - \frac{\partial q_z}{\partial z} + H_a + H_s + H_r \tag{4}$$

Where:

$$q_x = -k\frac{\partial T}{\partial x}, q_z = -k\frac{\partial T}{\partial z} \tag{5}$$

$$H_a = T\alpha_\rho \left(v_x \frac{\partial P}{\partial x} + v_z \frac{\partial P}{\partial z}\right) \tag{6}$$

$$H_s = \sigma'_{xx}\left(\varepsilon'_{xx} - \varepsilon'_{xx,elastic}\right) + \sigma'_{zz}\left(\varepsilon'_{zz} - \varepsilon'_{zz,elastic}\right) + 2\sigma'_{xz}\left(\varepsilon'_{xz} - \varepsilon'_{xz,elastic}\right) \tag{7}$$

In these equations, t is time, k is the thermal conductivity (W/(m·K)) and ρ is density. Both depend on temperature T and rock composition c. C_p is the isobaric heat capacity (J/mol), DT/Dt is the derivative of temperature with respect to time (Langrangian derivative), and q_x and q_z are the horizontal and vertical components of the heat flux (W/m^2), respectively. α_ρ is the thermal expansion coefficient (thermal expansivity, K^{-1}) and ε'_{ij} is the deviatoric strain rate tensor. H describes the different internal heating sources (e.g., the continental crust and its radioactivity). H_a is the adiabatic (de)compression, H_s is the shear heating during

nonelastic deformation, and H_r is the lithology-specific radioactive heat production. v_x and v_z are the horizontal and vertical velocities, respectively. σ'_{xx} and σ'_{xz} are the normal and shear components of the deviatoric stress tensor (Gerya and Yuen, 2007).

2.2. Constitutive equations

The governing relations previously described (see 2.1.) are solved here by using nonlinear viscoelastoplastic constitutive relations between deviatoric stresses and strain rates:

$$\epsilon'_{ij} = \frac{1}{2\eta}\sigma'_{ij} + \frac{1}{2G}\frac{D\sigma'_{ij}}{Dt} + \begin{cases} 0 & for\ \sigma'_{II} < \sigma_{yield} \\ \chi\frac{\partial g_{pl}}{\partial \sigma'_{ij}} & for\ \sigma'_{II} = \sigma_{yield} \end{cases} \tag{8}$$

Where ϵ'_{ij} is the deviatoric strain rate, σ'_{ij} is the deviatoric stress, η is the effective viscosity, G is the shear modulus, and t is the time. $\frac{D\sigma'_{ij}}{Dt}$ is solved using a time explicit scheme (e.g., Moresi et al. (2003)), it is the corotational time derivative. g_{pl} is the plastic flow potential, and χ is a plastic multiplier used to connect stresses and plastic strain rates. σ'_{II} is the second invariant of the deviatoric stress tensor described by $\sqrt{\sigma'^2_{xx} + \sigma'^2_{xz}}$. It is compared to the plastic strength σ_{yield}.

Viscosity is temperature-, pressure-, and stress-dependent and follows dislocation creep flow laws as described in Ranalli (1995):

$$\eta = \left(\frac{1}{\sigma'_{II}}\right)^{(n-1)} \cdot \frac{1}{2A_D} \cdot \exp\left(\frac{E_a + PV_a}{RT}\right) \tag{9}$$

Where n is the stress exponent, A_D is the preexponential factor, E_a the activation energy, and V_a the activation volume. These parameters are specific to each rock type. R is the gas constant (8.314 J/(mol·°C)).

2.3. Model Setup and initial conditions

The STM code represents a transect of a subduction margin that is 1500 km long and 200 km deep. Since The grid is composed of square-shaped cells; away from the subducting slab (i.e., region of interest), the grid size (i.e., size of a single cell) is at most 2,000 m while it is 500 m in the area of interest. The initial model setup consists of one continental plate and one oceanic plate (i.e., upper and lower crust, and lithospheric mantle) on top an asthenospheric mantle (Figure 4). The two plates are homogeneous, i.e., there is no pre-existing structure, and separated by a pre-existing sedimentary wedge and a weak zone cutting through the lithospheric mantle. The latter serves for the initiation of the subduction and has a very low plastic strength; it is later replaced by oceanic crust. The oceanic plate is pushed eastward at a constant convergence velocity of 40 mm/yr, while the continental plate is kept immobile. The lateral and top boundaries are free-slip boundaries while the bottom boundary is an open boundary that the slab can penetrate, it is also a free-slip at depth. An adiabatic geothermal gradient of 0.5°C/km is applied in the asthenosphere. The continental lithosphere has a linear gradient from 0 to 1300°C between the surface and 100 km depth. On the other hand, the temperature structure of the oceanic plate is calculated using the half-space cooling model (Turcotte and Schubert, 2012) from a constant plate age along the slab. All along the run of the model, the surface is being eroded at a rate of 3.0 mm/yr. Also, a phase change is allowed with the formation of serpentine at the megathrust.

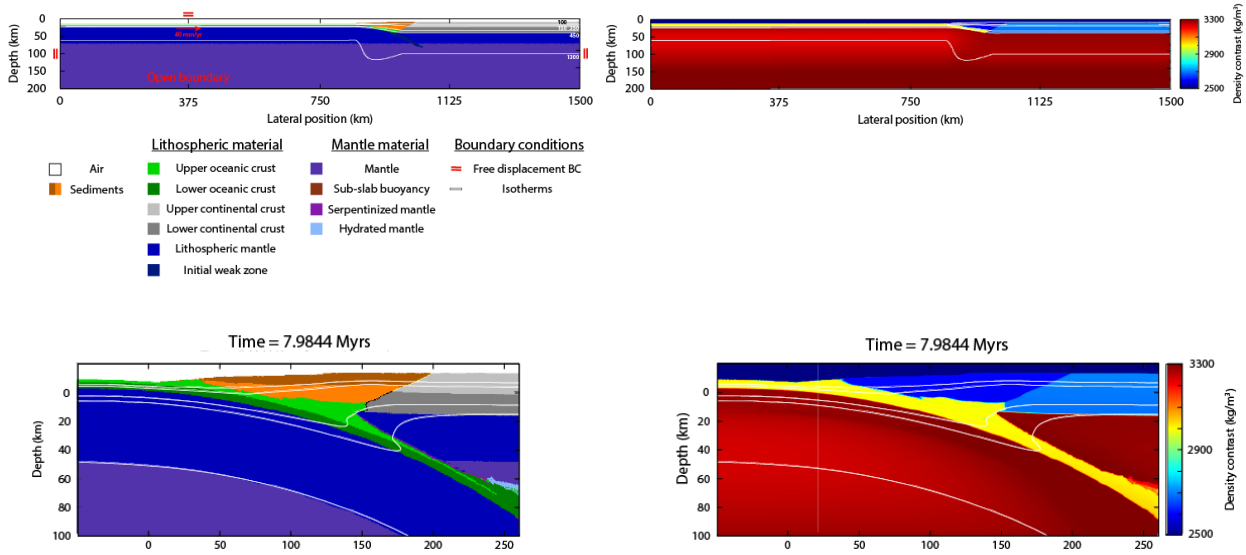

Figure 4: Model setup of the reference model without sub-slab density anomaly and a slab age of 11 Ma (reference model). (a) Rock composition at the first timestep. (b) Density of the materials at the first stimestep. (c) Rock composition at the last timestep. (d) Density of the materials at the last timestep. On each panel, the thin oceanic plate (left) is 11 Ma and moves at a velocity of 40 mm/yr to the East (right). To the right, in grey is the continental plate. In orange and brown are the sediments in the accretionary wedge, green are the oceanic crust components (including sediments in the upper crust with basalt). The dark blue dipping feature is the weak zone that allows the initiation of the subduction (present in (a) and (b)). The lithospheric mantle and the asthenospheric mantle can be distinguished by their color but they have the same properties. The x-axis indicates the lateral position in km from the left boundary of the model while the z-axis indicates the depth from the top of the thick air layer in km (top of the model).

2.4. Boundary conditions

I use a 2-D undeformable Eulerian mesh grid, so I add a 8- (continent) to 12.5-km (ocean) thick layer of "thick air" on top of the model to allow for topography to build (Crameri et al., 2012). This thick air material has a density of 1 kg/m^3, similar to air, and very low viscosity with respect to the material around (1.10^{17} Pa·s) acting as a free surface to prevent any shear stress from the atmosphere. To ensure a fully viscous behavior, its shear modulus is set to 700 GPa.

2.5. Short-term model

After a 258 timesteps in the long-term part of the model, the model transitions gradually to smaller timesteps, from 1,000 years to 5 years to be able to analyze earthquake sequences (i.e., coseismic and interseismic phases). The earthquake sequences are modeled by using rate-dependent friction that allows the detection of brittle instabilities simulating the brittle faulting at low temperatures and pressures as in subduction zones (van Dinther et al., 2013a).

The Rupture Detector Algorithm (RDA) developed by Dal Zilio et al. (2018) detects seismic events when a set of 3 markers undergo simultaneously a velocity slip rate of 6·10^{-9} m/s and a stress drop of more than 0.4 MPa. This algorithm also gives the hypocenter location of all events as well as their rupture widths, and the velocity along the slab at any point in time. The magnitudes of the earthquakes (3-D) are scaled from the rupture width (2-D) based on empirical scaling relationships (Blaser et al. (2010)).

2.6. Approach

To model the Cascadia subduction zone, I adapt the model setup for Southern Chile (van Dinther et al., 2013) to Cascadia. The benchmark model for Southern Chile is a 40 Ma Nazca plate converging with the South American plate at 75 mm/yr. Whereas the Juan de Fuca system is much younger, therefore, I build the reference model by choosing a plate age of 11 Ma which corresponds to Central Cascadia (Wilson, 2002) the segment supposedly not affected by any buoyancy effect. The convergence rate between the North maerican plate and the Juan de Fuca system is also much slower with a velocity of 40 mm/yr relatively constant along-strike (DeMets et al., 2010).

To model the three segments including the sub-slab buoyancy model proposed by Bodmer et al. (2018; 2020) and compare the impact of the different physical mechanisms proposed to cause lateral segmentation in Cascadia, I proceed to a parameter study of the following :

- Density contrast between the asthenosphere and the buoyant anomaly
- Position of the anomaly (depth and lateral position)
- Size of the density anomaly
- Plate age

First, I investigate the impact of a buoyant anomaly whose density contrast varies between 100 and 3.5 kg/m^3 for a slab of 11 Ma on the subduction zone. Next, I study the effects of varying plate ages with subducting slabs whose ages vary between 7.5 and 100 Ma. The ages tested include the two plate age models that have been proposed by Kelsey et al. (1994) and Wilson (2002):

- Kelsey et al (1994): 7.5 Ma – 18.8 Ma where along-strike plate age would be the main control on the segmentation of the subduction zone.
- Wilson (2002): 9 Ma – 13 Ma.

I also discuss the consequences on the subduction zone of varying initial lateral position of the density anomaly between 700 and 900 km from the left boundary and its size for areas (2-D) varying between 4,549 and 18,196 km^2.

I compare the outputs of these models in terms of subduction geometry (slab dip and slab curvature), topography, interseismic coupling, and seismicity to assess the viability of considering slab age as the main control on the along-strike segmentation of Cascadia.

The density anomaly impact is investigated in the sub-slab region on the subduction zone by, first, producing a reference Cascadia model that is representative of Central Cascadia with an age of 11 Ma and a convergence velocity of 40 mm/yr and without any anomaly in the sub-slab region. Next, I introduce the sub-slab buoyant anomaly by using mantle material with a fixed density at the bottom of the oceanic plate from the start of the model to minimize any flexure effect due to its rise. The buoyant anomalies have the same properties as the olivine-rich dry mantle as described in Ranalli (1995). I vary this initial density contrast between 3.5 kg/m^3, i.e., the minimum density contrast proposed by Bodmer et al. (2018; 2020) that illustrates the external layers of the Cobb hotspot entrained by the motion of the plate from the mid-ocean ridge, and 100 kg/m^3 as tested by Betts et al. (2012) representing a highly active mantle plume. The density contrasts are calculated as follows: $\Delta\rho = \rho_0 - \rho_d$ with $\Delta\rho$ the density contrast, ρ_0 the reference density of the surrounding mantle (3300 kg/m^3), and ρ_d the density of the buoyant anomaly. After 7.9 Myrs of buoyant rise during subduction these density contrasts effectively turn into anomalies between -29.2 and 42.9 kg/m^3 which is calculated by averaging the density of the asthenospheric and lithospheric mantle surrounding the density anomaly in a box extending from 700 to 990 km along the x-axis and from 60 to 170 km depth. The initial density of the buoyant anomaly is then

subtracted from the average density calculated. Bodmer et al. (2018; 2020) estimated the density contrast to be between 3.5 kg/m^3 and 10 kg/m^3. Once an approximate density contrast has been chosen based on a visual match with the conceptual model, I vary the position (depth and lateral position). This process allows me to provide constraints on a possible buoyant material lying in the sub-slab region below the seismogenic zone as proposed by Bodmer et al. (2018; 2020).

3. Results & Analysis

3.1. Sub-slab density anomaly

Two reference models are used to understand the effects of plate age variations and sub-slab buoyancy on the subduction zone, the parameters of the models are described in Table 1 below:

Reference model	Age of the oceanic plate (Ma)	Convergence velocity (mm/yr)	Density of the anomaly (kg/m^3)	Lateral position (km from left boundary)	Radius (km)	Depth (km from top of the model)	Shape
No buoyancy model	11	40	No anomaly	N/A	N/A	N/A	N/A
Sub-slab buoyancy model	11	40	3255	850	60	100	Circular

Table 1: Description of the parameters for both reference models (with and without buoyancy).

3.1.1. Evolution of the reference model with a sub-slab buoyancy

In the buoyancy models, at a time of 0 My a circular sub-slab density anomaly with a radius of 60 km, whose density is 3255 kg/m^3 is placed amidst a mantle density of 3300 kg/m^3, is located 850 km from the left boundary and 100 km from the top boundary (Figure 5). The location of the sub-slab buoyant anomaly was chosen to match the conceptual model proposed by Bodmer et al. (2018; 2020), which describes a sub-slab buoyant anomalies in Northern and Southern Cascadia as independent mantle upwellings below at the hinge ifof the slab below the seismogenic zone. However, due to its buoyancy, it does not sink with the slab and remains at the hinge of the slab below the seismogenic zone.

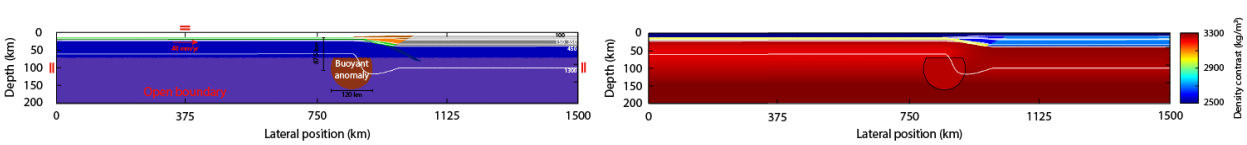

Figure 5: Initial setup of the reference model for sub-slab buoyancy models (11 Ma, 45 kg/m^3 of density contrast). (a) Rock composition of the initial setup (see Figure 4 for the name of each rock type). (b) Initial density of the different rock types. The white lines are the isotherms. The x-axis is the horizontal distance from the left boundary, and the y-axis is the vertical distance from the top boundary.

After 2.83 Myrs, the anomaly has deformed, flattened, and risen up against the slab, applying a vertical force on it (the buoyancy force) reducing the curvature of the slab in the mantle (Figure 6). One can observe that, at the hinge of the slab (X ~ 50 km), the density of the plate seems to decrease slightly.

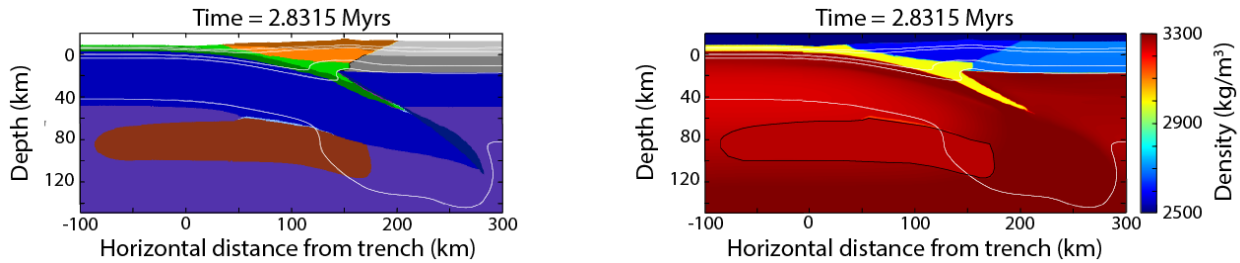

Figure 6: Reference model for sub-slab buoyancy models (11 Ma, 45 kg/m^3 of density contrast) after 2.83 Myrs. (a) Rock composition (see legend Figure 4). (b) Density of the different rock types. The white lines are the isotherms 100, 150, 350, and 450°C. In all figures from here on, the x-axis is the horizontal distance from the trench in this reference model (X = 830.7 km), and the y-axis is the vertical distance from the trench in this reference model (Y = 13.907 km).

After 5.83 Myrs, part of the buoyant anomaly has been entrained at depth during subduction. The anomaly flattens the slab at depth, although most of it remains stuck at the hinge of the subducting slab below the seismogenic zone (Figure 7).

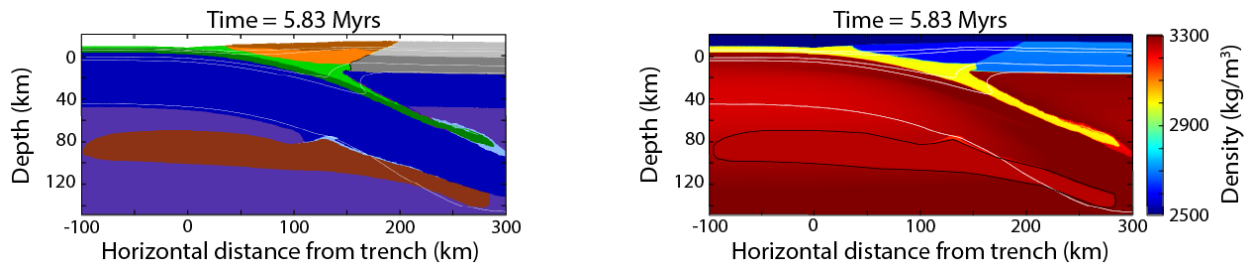

Figure 7: Reference model for sub-slab buoyancy models (11 Ma, 45 kg/m^3 of density contrast) after 5.83 Myrs. (a) Rock composition (see Figure 4 for the name of each rock type). (b) Density of the different rock types. The white lines are the isotherms 100, 150, 350, and 450°C. The x-axis is the horizontal distance from the trench, and the y-axis is the vertical distance from the trench.

After 7.9 Myrs, part of the density anomaly has been brought to depth by the motion of the slab while the rest has stabilized at the hinge of the slab. The effective density contrast is calculated at this last timestep from the red box (Figure 8b). For 45 kg/m^3 of initial density contrast, the effective density contrast is 4.1 kg/m^3. For the other density contrasts, the effective density contrast tends to be ~44 kg/m^3 lower than the initial density contrast, on average.

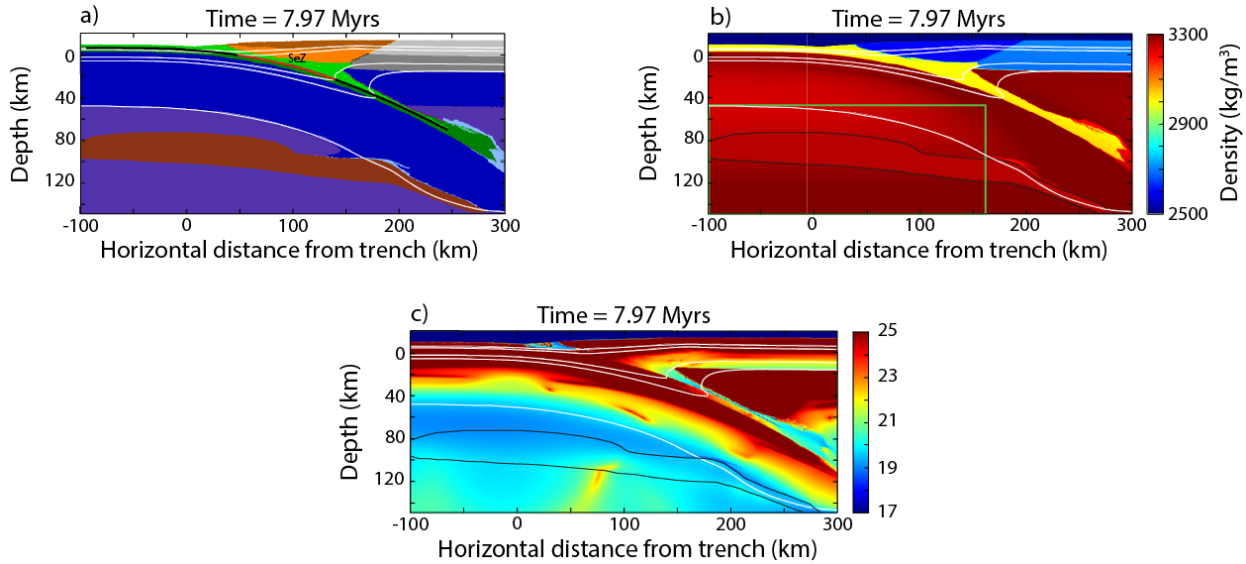

Figure 8: Reference model for sub-slab buoyancy models (11 Ma, 45 kg/m^3 of density contrast) after 7.9 Myrs. (a) Rock composition (see Figure 4 for the name of each rock type). The black continuous line highlights the interface between the upper and lower crust of the oceanic plate that I used to calculate slab dip. The red part of the black line is the seismogenic zone defined as the section of the megathrust between the 150 and 350°C isotherms (b) Density of the different rock types. (c) Viscosity. The white lines are the isotherms 100, 150, 350, and 450°C. The x-axis is the horizontal distance from the trench, and the y-axis is the vertical distance from the trench. The green box in (b) shows the limits of the box where the average density around the buoyant anomaly is being calculated. The black contours in (b) and (c) show the contours of the sub-slab anomaly.

Buoyant anomalies with lower densities tend to rise faster and more against the slab, whereas, for higher densities, they tend to flatten, not rise, and getting less entrained by the slab.

3.1.2. Variations in density contrast

a. Slab dip

Model simulations reveal a strong decrease of slab dip at geodynamic depths (defined from 45 to 70 km below the trench of the reference model without buoyancy (Fig. 8b)) with increasing density contrast (R^2 = 0.926, Fig. 9.). The trend at the seismogenic zone (defined from 4 to 20 km below the trench of the reference model without buoyancy) is weaker (R^2 = 0.337) but indicates a steepening of the slab with the introduction of higher density contrasts (Fig. 9b). Variations in slab dip seem to be twice as large at geodynamic depths (5-6 degrees) than at the seismogenic zone (2-3 degrees). Slab curvature seems to be generally higher at geodynamic depths than it is at the seismogenic zone.

It is more difficult to describe the apparent slab curvature trends confidently due to low R^2, but the slab curvature seems to be slightly increasing at the seismogenic zone and slightly decreasing at geodynamic depths for high density contrasts. Therefore, these results agree with the slab dip results because, at the seismogenic zone, for higher density contrasts, the slab steepens and the slab bends more, while at geodynamic depths, the slab dip tends to be shallower because the slab unbends. One can notice that the higher the density contrast, the further the center of the anomaly gets dragged to the right.

I interpret here that, at geodynamic depths, a higher density contrast induces a shallower slab dip because the anomaly does not interact as much with the mantle wedge as it does with the continental plate at the seismogenic zone., Tthe mantle wedge is behaving fully viscously so it is much easier for the anomaly to push the tip of the slab upward and, therefore, unbending the slab. The tip of the slab is mostly sensitive to the extremity of the sub-slab anomaly. Contrary to geodynamic depths, the slab steepens at the seismogenic zone

for a higher density contrast. At the seismogenic zone, the slab is mostly affected by the center of the anomaly located to the left of the seismogenic zone. Therefore, because of of the applied upward push left of the seismogenic zone, the trench is pushed upward and to the right, resulting in a rotation of the slab at the seismogenic zone toward steeper slab dips. This effect intensifies as the density contrast gets higher because the buoyancy force depends on the density contrast between the buoyant anomaly and the surrounding mantle. Also, as the density contrast gets higher, i.e., the density of the anomaly is lower, its viscosity is also lower resulting in a stronger entrainment to depth by the slab.

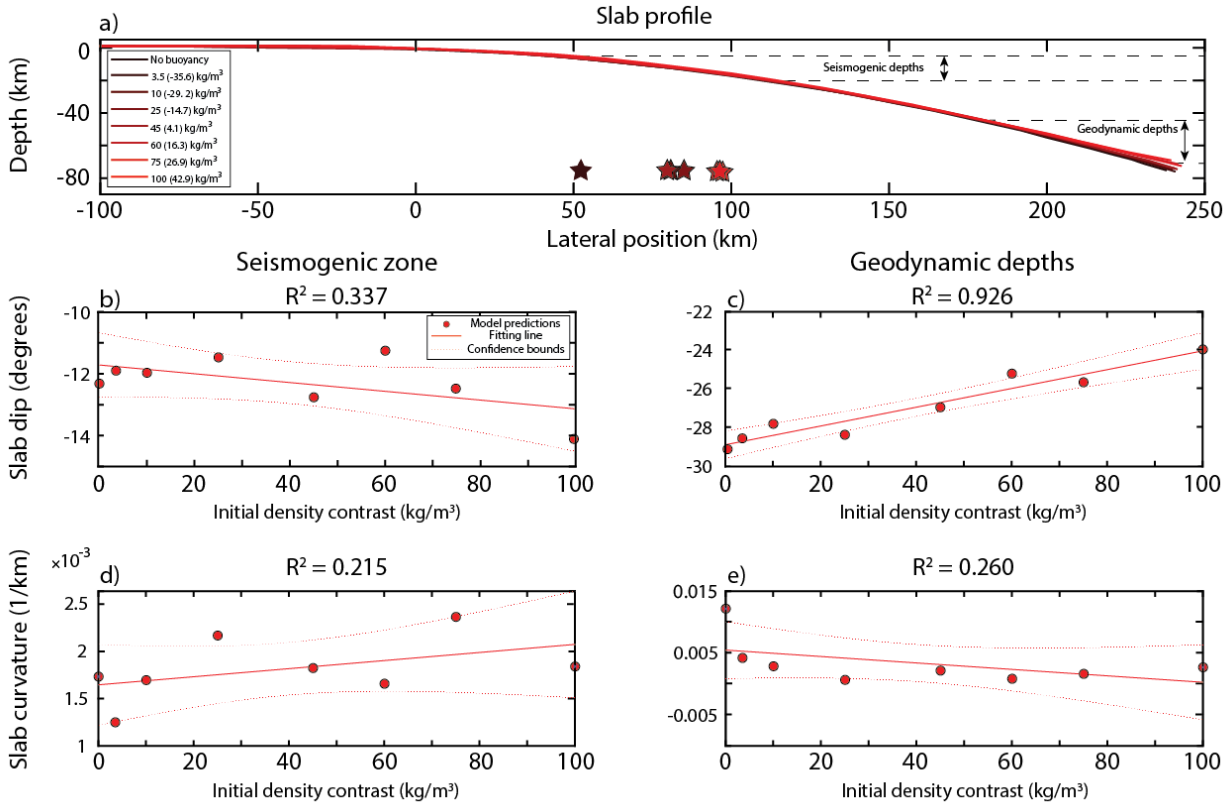

Figure 9: Slab profile (a), slab dip (b-c) and apparent slab curvature (d-e) for different density contrasts at t = 7.9 Myrs. (a) Stars indicate the horizontal center of the anomaly at the last timestep. The dashed lines delimit the seismogenic zone and the geodynamic depths areas of calculation of the slab dip and the slab curvature. I measured slab dip and slab curvature in restricted areas of the subduction zone (4-20 km and 45-70 km) to maximize the variations observed, whereas, in reality, the seismogenic zone can extend down to about 40 km. Between parentheses are the effective desnity contrasts. (b-c) Seismogenic zone (b) and geodynamic depths (c). The less negative the value is, the shallower the slab dip is. (d-e) Seismogenic zone (d) and geodynamic depths (e). (b-e) The red dots are the model results, while the red lines are the linear regressions that fit the predictions best estimated using a root-mean-square (RMS) error method where $R^2 = 1$ is the best fit, the dashed lines are the 95% confidence bounds of the regression line. Slab curvature is calculated using circfit (Andrew Horchler (2022). Circfit (https://github.com/horchler/circfit), GitHub. Retrieved June 8, 2022) to extract the bending radius of the slab and obtain the slab curvature from 1/R where R is the bending radius (Turcotte and Schubert, 2012). Results are said to be at the seismogenic zone when they are averaged between 4 and 20 km deep and they are said to be at geodynamic depths when they are averaged between 45 and 70 km deep.

b. Topography

Simulations show that the higher the density contrast, the higher the topography is in the forearc region (X~150 – 200 km) (Fig. 10a), it is about 700 m higher for 42.9 kg/m^3 of effective density contrast than when the anomaly is absent (Fig. 10b).Regarding the oceanic plate, one can argue that the stronger the density contrast the higher the seafloor lies with respect to the reference model and the more the trench is displaced to the

right (Fig. 10c, d). For instance, for the highest density contrast, the seafloor lies a few ~100 m above the reference position and the trench is located ~10 km to the right of the reference trench location (Fig. 10c, d). One may notice that the highs in topography in the overriding plate are located on or close to the largest variations in slab depth but the changes in the topography are reduced relatively to the slab depth changes. This can illustrated by looking at the strongest density contrast where the two peaks of ~500-700 m of uplift between a 150 and 200 km from the trench in the overriding plate correspond to ~1.7-2.0 km in slab depth (Fig. 10b,d).

Since the buoyant anomaly pushes upward onto the slab (see 3.1.2.a., Bodmer et al. (2018; 2020)), the slab is elevated such that it displaces the location of the trench as well resulting into a higher pressure at the interface between the subducting slab and the overriding plate. By increasing the pressure at the interface, the overriding plate undergoes a compressional force that induces shortening and topography buildup. Interestingly, a rise in vertical position of the slab of 1.5 km does not reflect the exact same variation in the topography of the overriding plate but only 500 m of uplift (Fig. 10b,d). This suggests that the overriding plate deforms and thins either internally in an inelastic fashion (e.g., in the overriding lower crust) or elastically as a whole to accommodate the additional push from the anomaly from below. Regional, elastic deformation can be understood through regional isostasy or flexure (Stuwe (2007); Turcotte and Schubert (2012)), where the continental lithosphere is considered as a strong, elastic beam able to distribute stresses over larger areas. Beyond 200 km from the trench, the slab becomes exponentially shallower because it enters the mantle wedge which behaves fully viscously, to accommodate the change in position of the slab, it thins inelastically without transferring the upward push to the overriding plate.

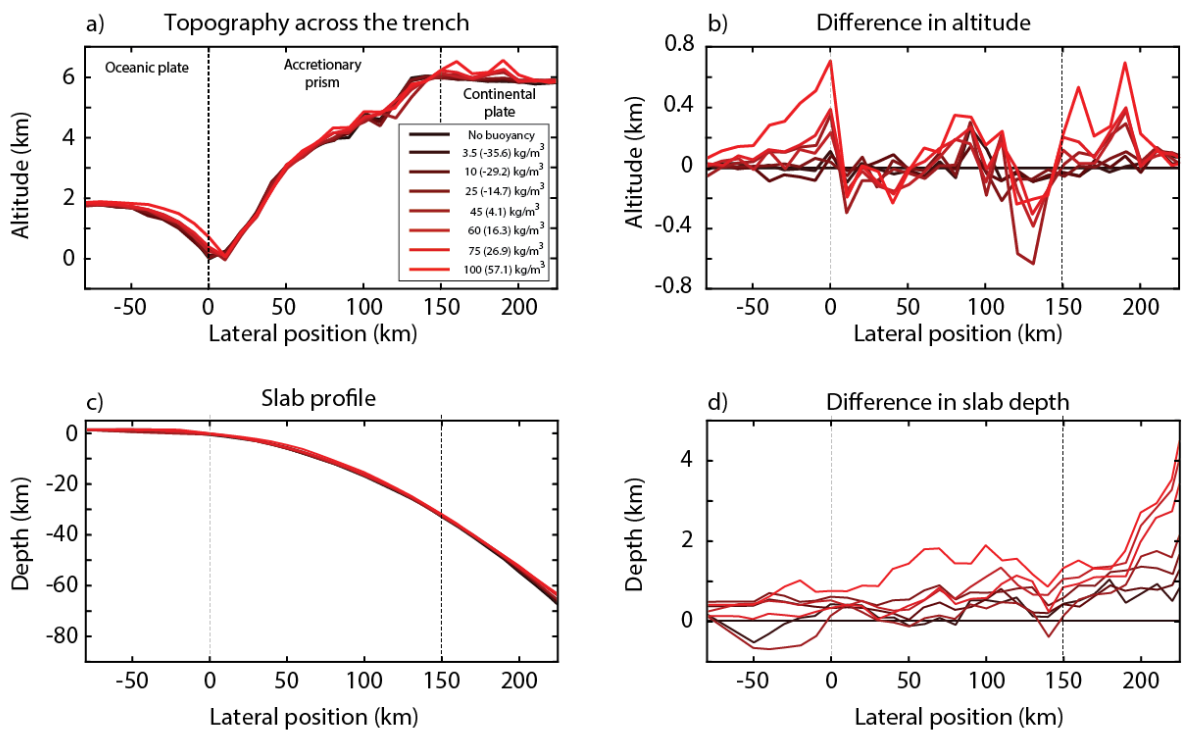

Figure 10: Topography (a-b) and slab profiles (c-d) for varying density contrasts. (a) Altitude with respect to the trench at the isostatic equilibrium for varying density contrasts. Dashed lines are the limits between the oceanic plate and the accretionary prism, and the accretionary prism and the continental plate. Between parentheses are the effective density contrasts. (b) Changes in topography with respect to the reference model. (c) Slab profiles for varying density contrasts corrected for isostatic equilibrium to have an initial depth of 0 for all models. (d) Variations in vertical position of the slab with respect the reference model .

c. Earthquake sequences

The seismic sequence is composed of three main phases: the interseismic period (accumulation of strain, stress buildup), the coseismic phase (elastic rebound during the earthquake), and the postseismic period (viscoelastic relaxation and afterslip). Here, I focus on the interseismic period studying the interseismic coupling, and the coseismic phase investigating the rupture width distribution the impact of the sub-slab buoyancy on the interface between the two plates.

Interseismic coupling

Simulations show that, during the interseismic periods (gray-to-white colors, Figure 11a,b), the overriding plate moves toward the continent (darker gray), i.e., the same direction as the subducting slab indicating a coupling of the two plates. One can observe that, at the updip limit of the seismogenic zone, i.e., between 0 and 100 km from the trench, the higher the density contrast, the closer to the trench the gray area is (Fig. 11a,b), so the less the upper plate moves toward the continent. This agrees with the interseismic coupling that shows, for the same range distance from the trench, a lower coupling as the higher density contrast increases (Fig. 11c). In the downdip region (~140+ km), however, the upper plate tends to move more towards the continent when a higher density contrast is introduced in the model (Fig. 11a,b). This also agrees with the interseimsic coupling that increases with higher density contrasts (Fig. 11c). Therefore, the higher density contrast, the less coupled are the plates at the updip limit of the seismogenic zone and the more coupled they are at the downdip limit of the seismogenic zone. For higher density contrasts, one can observe that the earthquakes tend to nucleate in a relatively narrow area close to 120 km away from the trench while in lower density contrasts models, the location of the hypocenters tend to be heterogeneous.

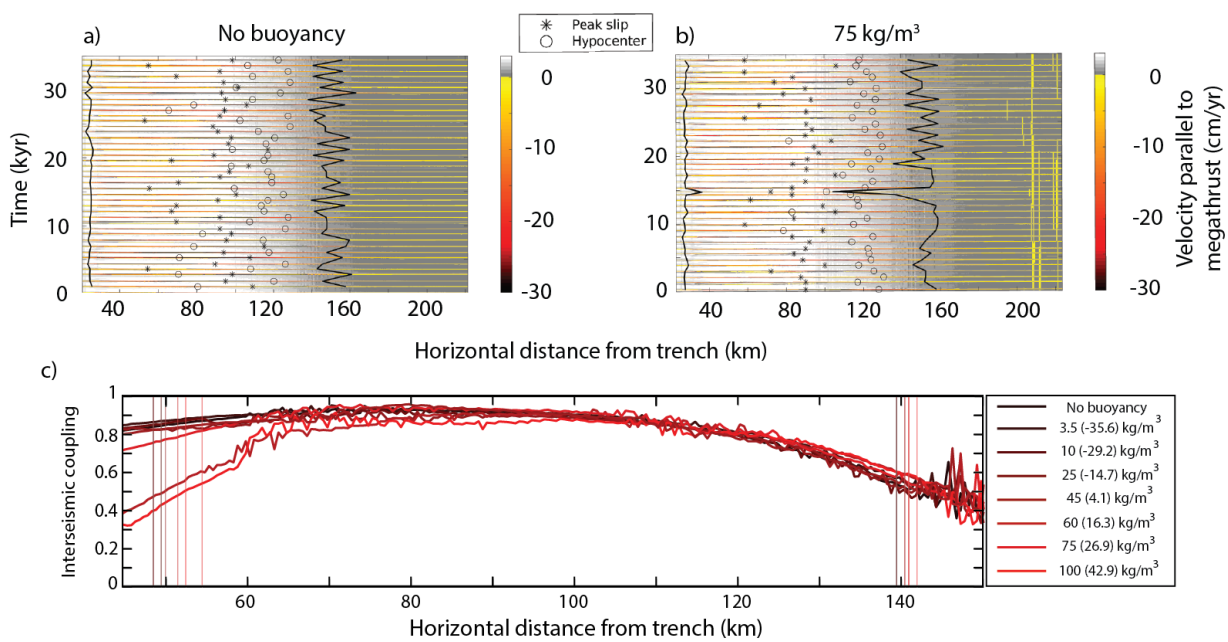

Figure 11: Velocity parallel to the megathrust (a-b) and interseismic coupling (c). (a-b) Velocity parallel 6.4 km above the megathrust (overriding plate) for the reference model (a) and 26.9 kg/m³ of effective density contrasts (b). Velocities are positive (gray-white) towards the continent. Continuous black lines are the limits of the ruptures for each event. Circles are hypocenter locations and stars are the peak slip locations. (c) Interseismic coupling for different density contrasts. Calculated by the ratio of velocities at 6.4 km above and below the megathrust, 1 is the theoretical value for two fully coupled plates. The vertical lines are the up- and downdip limits of the seismogenic zone based on the 150 and 350ºC isotherms. Between parentheses are the effective density contrasts.

When monitoring plastic and viscous strain rates, one can observe that the plastic behavior in the overriding plate for a higher density contrast tends to extend closer to 60 km than the reference model without buoyancy (Fig. 12c,d). At depth, one can observe that higher density contrasts show slightly lower viscous strain rates over a slightly narrower extent (Fig. 12g,h).

Plastic and viscous strain rates reflect the behavior of deformation along the megathrust, i.e., the higher the visco-plastic strain rates, the more creeping the megathrust is. Therefore, my simulations show that, in the updip region, the megathrust tends to creep over a slightly larger region for higher density contrast, but brittle behavior is observed until slightly deeper at the downdip limit. This is supported by the velocities in the overriding plate parallel to the megathrust that show a higher displacement towards the continent (Fig. 11a,b) and a higher coupling between the plates (Fig. 11c) at the updip (Figure 11a, b) for the reference model. On the other hand, at depth, in the downdip region, where the subduction channel is warmer and thus behaves more ductile, the displacement (Fig. 11a,b) and the coupling (Fig. 11c) is higher for the higher density contrasts which is followed by a decrease in the extent of viscous behavior in favor of brittle behavior (Fig. 12g,h). This shows that the higher the density contrast, the lower the coupling between the plates at the updip limit of the seismogenic zone but the higher the coupling is at the downdip limit.

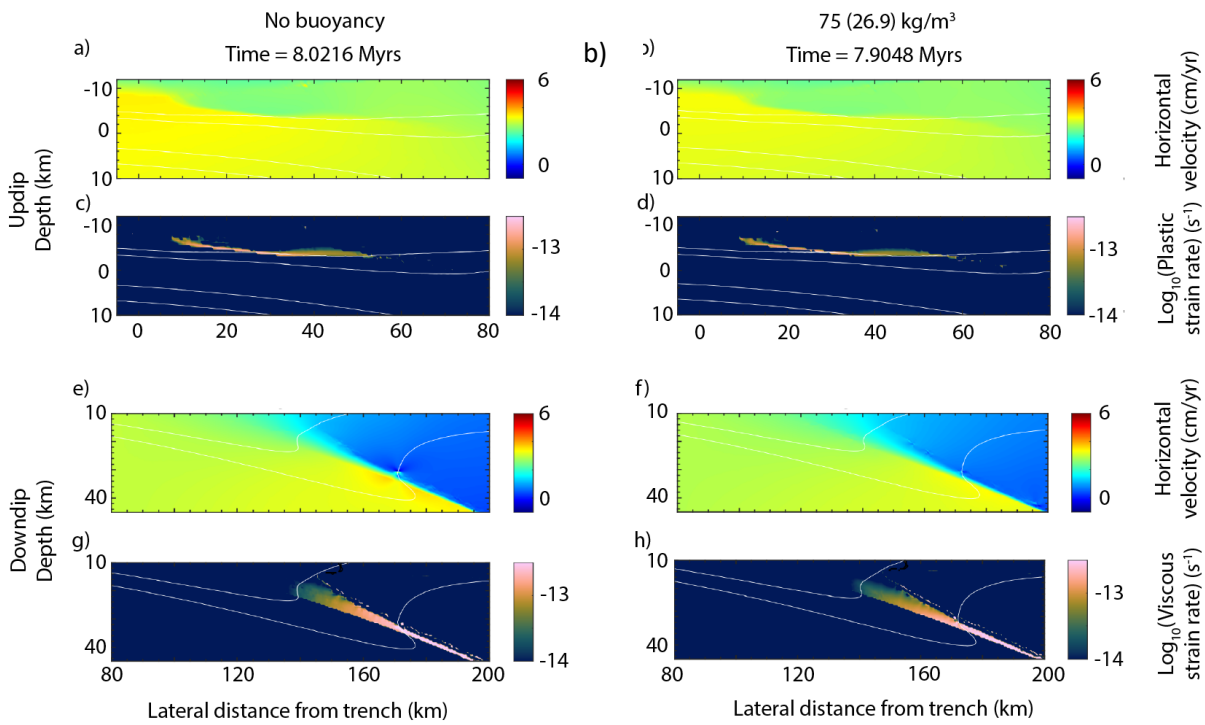

Figure 12: Visco-plastic strain rates at the megathrust for different density contrasts. (a-d) Snapshot of horizontal velocity (a-b) and plastic strain rate (lower c-d) in the updip region. The plastic strain rates are displayed in a log scale. The white lines indicate the 100°C, 150°C, 350°C, and 450°C isotherms. (e-h) Snapshot of horizontal velocity (e-f panel) and plastic strain rate (g-h) in the downdip region. The white lines indicate the 350°C and 450°C isotherms. (a, c, e, g) Reference model. (b, d, f, h) Buoyancy model with 26.9 kg/m³ of effective density contrast.

Rupture widths

During the coseismic phase, earthquakes nucleate, and ruptures propagate. When considering increasing density contrasts, rupture widths tend to decrease from 70-80 km to a bimodal distribution around shallower widths of 10-20 km and 50-70 km (Fig. 13). Therefore, a higher density contrast induces narrower rupture

widths. As the rupture width decreases with an increasing density contrast, the number of ruptures increase from 58 for the reference model in total to 74 for an effective density of 42.9 kg/m^3.

The decrease in rupture width and thus size of the ruptures with density contrast can be explained by the steepening of the slab and the increase in slab curvature with density contrast (Figure 9). As a matter of fact, Heuret et al. (2011) show that, for a steeper slab dip, ruptures tend to propagate over shorter distances. Also, Bletery et al. (2016), showed that increased slab curvature tends to limit the propagation of ruptures due to the presence of more heterogeneities along the interface, so their extent decreases with higher slab curvature and the megathrust can rupture more often.

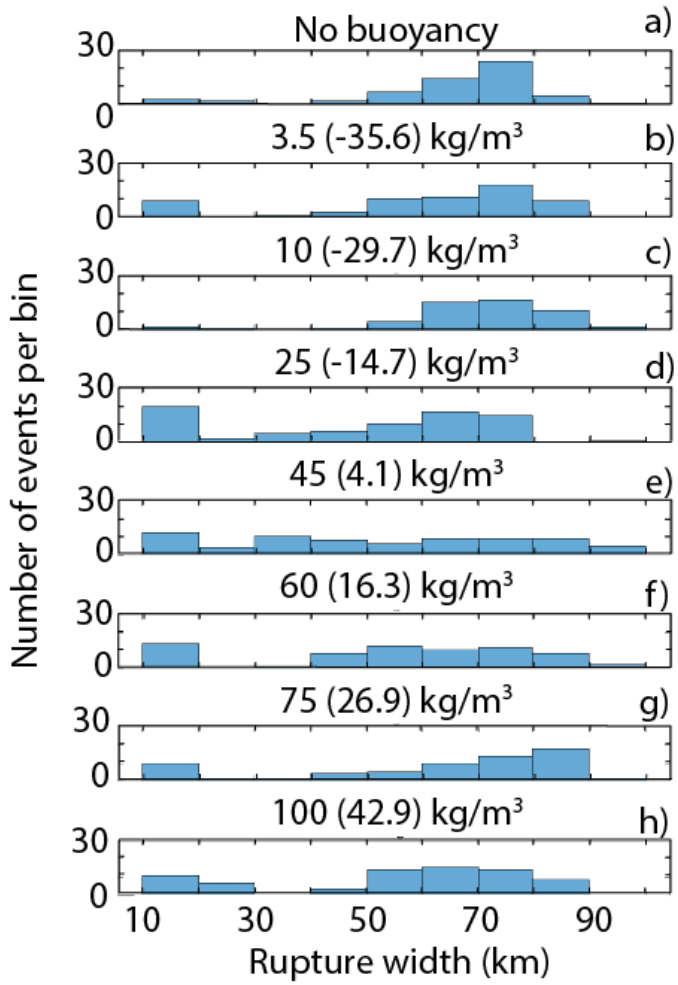

Figure 13: Rupture width distribution for varying density contrasts. Panels are ordered from no buoyancy (reference model) anomaly (a) to the highest density contrast (h). In parentheses are the effective density contrasts. The x-axis represents the rupture width of the events binned into 10-km bins and the y-axis is the density of events per bin. Between parentheses are the effective density contrasts.

3.1.3. Location of the anomaly

The lateral position of the density anomaly studied here refers to the initial location of its center with respect to the left boundary. I vary this from 700 to 900 km.

a. Slab dip

My results indicate that there is no apparent correlation between the slab dip at the seismogenic zone and the initial lateral position of the anomaly (Fig. 14b). However, it has a much stronger impact at the geodynamic depths where the slab dip is 10 degrees shallower for an initial position of 900 km from the left boundary than it is for an initial position of 700 km (Fig. 14c). On the other hand, the slab curvature decreases at the seismogenic zone for an initial position closer to the trench (900 km) (Fig. 14c) and almost doubles at geodynamic depths from an initial position of 700 km to 900 km (Fig. 14d). The final location of the center of the anomaly depends on its initial location, the closer it is to the trench, the more the anomaly is entrained at depth by the motion of the slab (Fig. 14a).

The closer to the trench the anomaly is located initially, the shallower the slab dip is at geodynamic depths because it tends to interact with the slab earlier in the subduction process. Therefore, the buoyant force is applied longer onto the tip of the slab which allows to deform and flatten it which induces an unbending of the slab at depth. This may seem contradictory for a slab curvature increase at geodynamic depths, but it is explained by the fact that it is only the tip that flattens. In the meantime, the rest of the slab, by flexure, must accommodate the slab dip at the seismogenic zone and the flattening of the tip resulting in a slab that is convex at the seismogenic zone and relatively concave at the tip. Consequently, due to flexure, the slab curvature at the seismogenic zone decreases because of the general upward push of the plate that makes the deeper parts of the plate lie at shallower depths.

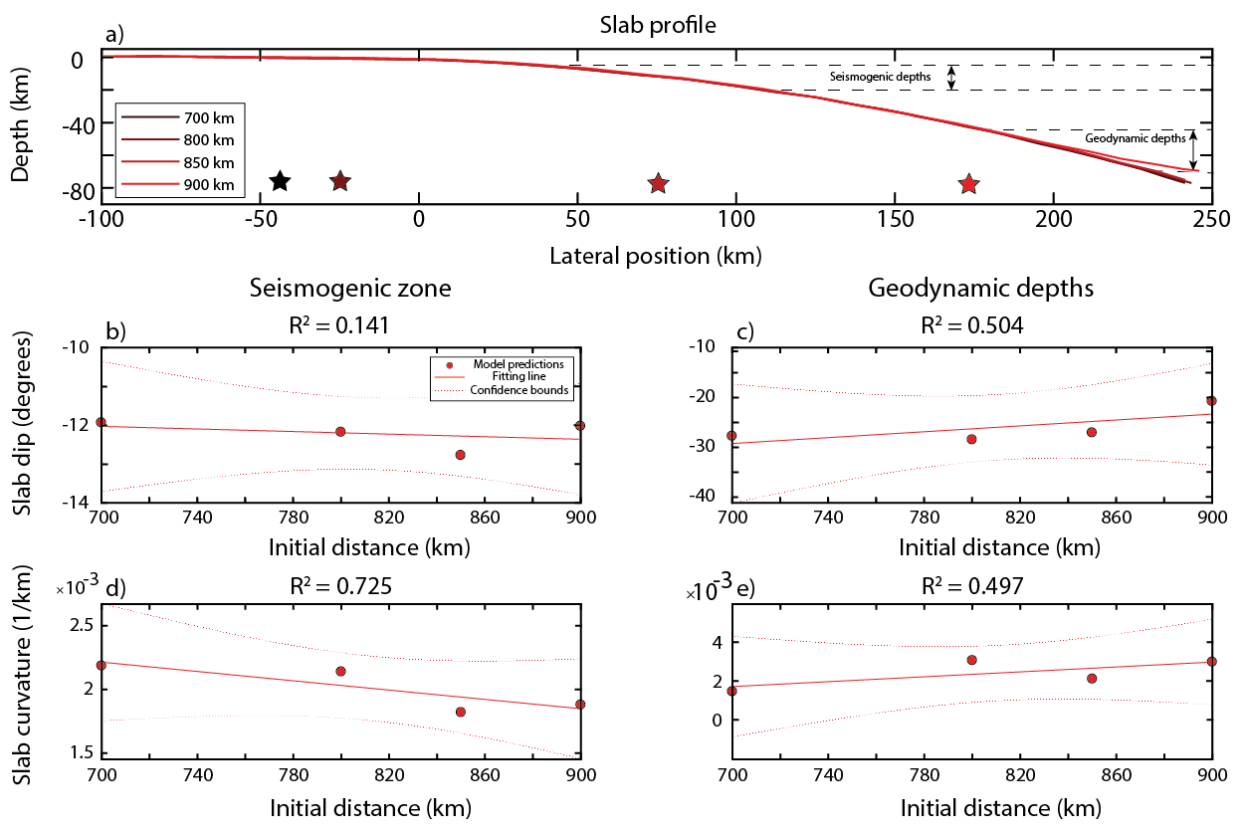

Figure 14: Slab profile (a), slab dip (b-c) and apparent slab curvature (d-e) for different initial locations of a density anomaly with an effective density contrast of 4.1 kg/m^3 at t = 7.9 Myrs. (a) Stars indicate the horizontal center of the anomaly at the last timestep. The dashed lines delimit the seismogenic zone and the geodynamic depths areas of calculation of the slab dip and the slab curvature. (b-c) Seismogenic zone (b) and geodynamic depths (c). The less negative the value is, the shallower the slab dip is. (d-e) Seismogenic zone (d) and geodynamic depths €. (b-e) The red dots are the model results, while the red lines are the linear regressions that fit the predictions best estimated using a root-mean-square (RMS) error method where R^2 = 1 is the best fit, the dashed lines are the 95% confidence

bounds of the regression line. Slab curvature is calculated using circfit (Andrew Horchler (2022). Circfit (https://github.com/horchler/circfit), GitHub. Retrieved June 8, 2022) to extract the bending radius of the slab and obtain the slab curvature from 1/R where R is the bending radius (Turcotte and Schubert, 2012).

b. Topography

The models show that the trench is displaced to the right of about 10 km at the farthest for the closest anomaly (900 km) relative to the reference position of the trench (Fig. 15a). For the anomaly that is located the closest to the trench initially, one can observe that a bulge in the forearc topography is created with a relative altitude of 450 m with respect to the reference model without buoyancy (Fig. 15b). Note that this bulge does not exist in the reference model (Fig. 15a) and its height increases when the anomaly is located closer to the trench (Fig. 15a,b). The changes in topography correlate relatively well with the extrema in the slab vertical position changes but in reduced magnitudes (Fig. 15b,d). For instance, the left peak of ~400 m around 175 km in the topography (Fig. 15b) corresponds to a slab depth change of ~1.5 km (Fig. 15d).

When the anomaly is set closer to the trench, the trench is displaced to the right because of the upward motion of the slab induced by the buoyancy force of the anomaly, while the initial location and structure of the overriding plate is never changed, so the pressure at the interface increases. This increase in pressure at the trench leads to more deformation (shortening and topography) of the overriding plate. The relation between slab depth changes and topography changes suggest that the buoyancy force pushes the slab upward which also pushes against the overriding plate but the buoyancy force is partially absorbed by the strength of the elastic overriding plate or the non-elastic behavior of the lower crust which tends to be weaker and more viscous than the rest of the plate (Fig. 8c). However, I am not able to determine whether the larger absorption of the force is carried by the strength of the lithosphere or the non-elastic behavior of the lower crust. For distances from the trench of more than 200 km, an exponential shallowing of the slab depth panel which has no- to low-effect on the topography of the overriding plate because the plate is in the mantle wedge which acts fully viscously and, therefore, flows to accommodate this change in position of the slab.

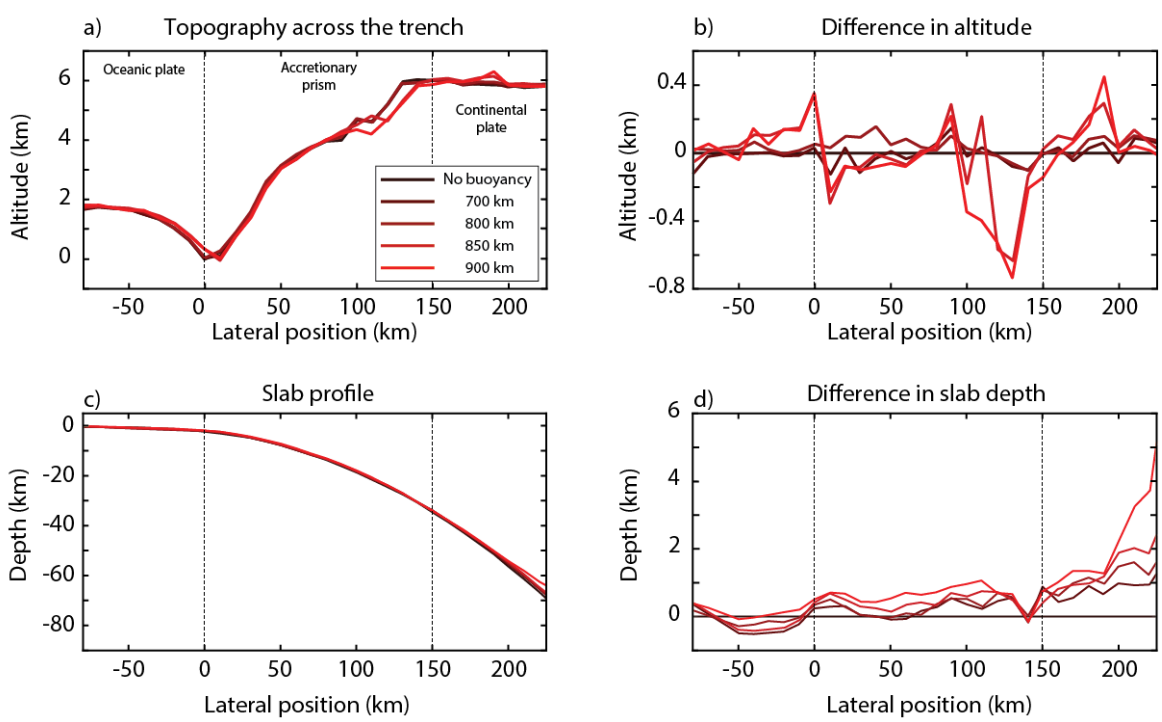

Figure 15: Topography (a-b) and slab profiles (c-d) for varying initial positions of the sub-slab density anomaly from the left boundary for an effective density contrast of 4.1 kg/m³ at t = 7.9 Myrs. (a) Altitude with respect to the trench at the isostatic equilibrium. b) Changes in topography. (c) Slab profiles f. (d) Variations in vertical position of the slab.

c. Earthquake sequences

Interseismic coupling

Results indicate that for anomalies initially located closer to the trench, the overriding plate during the interseismic period moves slower to the right, i.e., the direction of motion of the subducting slab, in the updip region (~110 km from the trench) (Fig. 14a, b). At depths, however, in the downdip region (~140 km from the trench) the closer the anomaly is initially to the trench, the faster it moves to the right of the model with respect to the velocity in the overriding plate when the anomaly is initially located further away from the trench (Fig. 14a,b). One may also notice that the closer the anomaly is initially to the trench, the more hetergeneous the location of the hypocenters is as well as the rupture widths (Fig. 16a,b). Nevertheless, overall, closer anomalies seem to produce narrower extents of the seismogenic zone (Fig. 16a,b).

These velocities differences agree with the interseismic coupling that seems to decrease as the slab is initially set closer to the trench in the updip region (distances lower than 70 km from the trench) (Fig. 16c). In the downdip region (distances beyond 120 km from the trench), the coupling increases as the anomaly is located closer to the trench at the start of the model (Fig. 16c). One can also argue that when the anomaly is located far away from the trench, it tends to interact much less or not at all with the slab as the interseismic coupkling suggests with little variations between the no buoyancy model and that with a buoyancy located at 700 km from the left boundary, i.e., the furthest from the trench (Fig. 16c).

My results suggest that the closer the anomaly is initially located to the trench, the more the plates tend to creep past each each other in the updip region, while the presence of the anomaly closer to the trench tends to lock them in the downdip region.

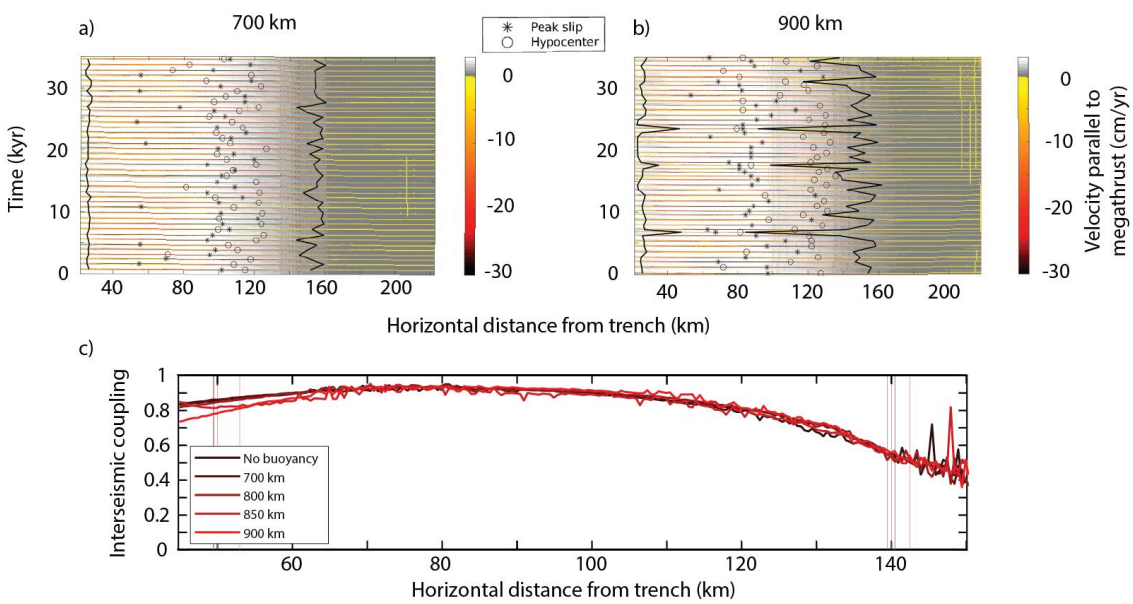

Figure 16: Velocity parallel to the megathrust (a-b) and interseismic coupling (c). (a-b) Velocity parallel 6.4 km above the megathrust (overriding plate) for the reference model (a) and 4.1 kg/m³ of effective density contrasts (b). Velocities are positive (gray-white) towards the continent. Continuous black lines are the limits of the ruptures for each event. Circles are hypocenter locations and stars are the peak slip locations. (c) Interseismic coupling for different density contrasts. Calculated by the ratio of velocities at 6.4 km above

and below the megathrust, 1 is the theoretical value for two fully coupled plates. The vertical lines are the up- and downdip limits of the seismogenic zone based on the 150 and 350°C isotherms. Between parentheses are the effective density contrasts. The vertical lines are the up- and downdip limits of the seismogenic zone based on the 150 and 350°C isotherms.

Plastic strain rates in the updip region show a slight increase in length (a few km) for a closer anomaly (Fig. 17b,d). On the other hand, viscous strain rates show lower values and a slight decrease in the length of the viscous region than for the reference model (Fig. 18f,h).

Therefore, the correlation between a slower displacement towards the continent and the larger extent of the plastic behavior (i.e., more creep at the interface) at the updip limit of the seismogenic zone confirm the lower coupling observed in the updip region for closer anomalies. On the other hand, at the downdip limit, the larger displacement towards the continent and the lower viscous strain rate values as well as the smaller extent of the viscous region support the higher coupling observations between the plates at the downdip limit. (see 3.2.1.c)

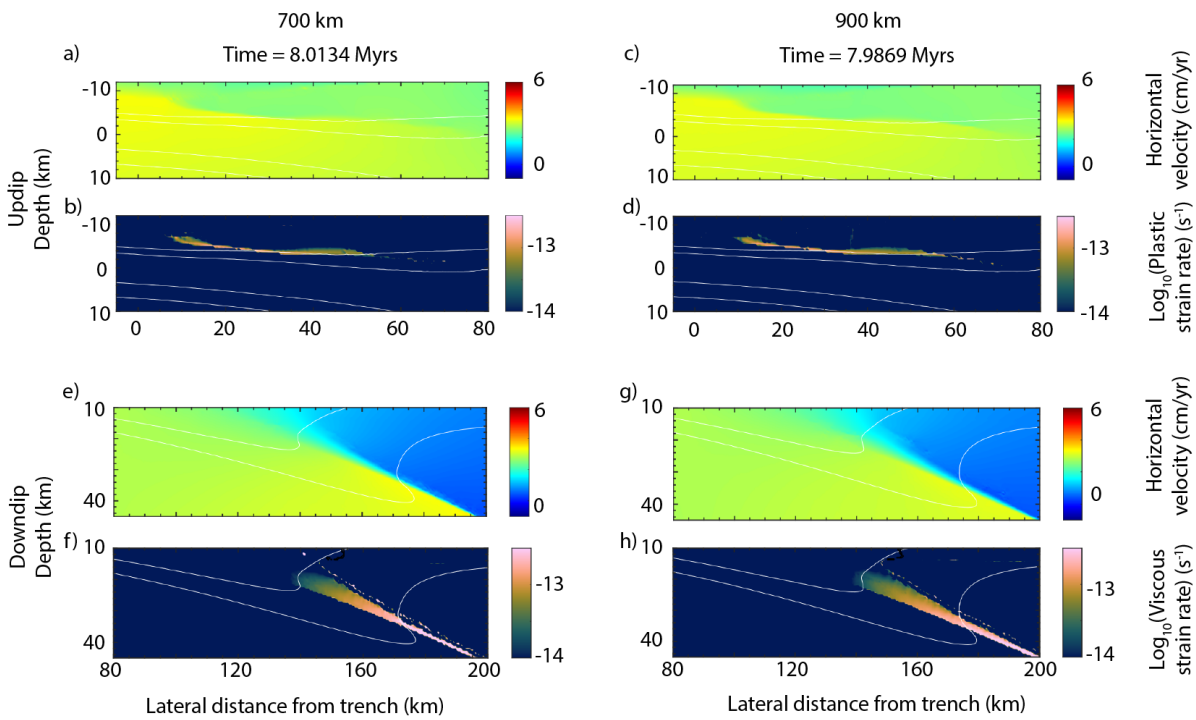

Figure 17: Visco-plastic strain rates at the megathrust for different initial positions of the sub-slab buoyant anomaly with an effective density contrast of 4.1 kg/m³. (a-d) Snapshot of horizontal velocity (a-b) and plastic strain rate (lower c-d) in the updip region. The plastic strain rates are displayed in a log scale. The white lines indicate the 100°C, 150°C, 350°C, and 450°C isotherms. (e-h) Snapshot of horizontal velocity (e-f panel) and plastic strain rate (g-h) in the downdip region. The white lines indicate the 350°C and 450°C isotherms. (a, c, e, g) Reference model. (b, d, f, h) Buoyancy model with 26.9 kg/m³ of effective density contrast.

Rupture widths

In terms of seismicity, the closer the anomaly is located to the trench, the more frequent is the seismicity and the more heterogeneous are the rupture extents (Fig. 18). As a matter of fact, only 58 events are detected in the 700 km model while 74 are described in the model where the anomaly is initially located 900 km away from the left boundary. Also, the rupture widths tend to be more evenly distributed the closer the anomaly is located to trench while they tend to center around 60-80-km bins of width when the anomaly is further away (Fig. 18).

When the initial position of the anomaly is closer to the trench, the seismicity becomes more frequent and the rupture widths tend to be more evenly distributed, however, it remains unclear why this happens and needs further investigation on the state of stress of the slab. As a matter of fact, when the anomaly is closer to the trench, it tends to unbend at depth creating a secondary hinge in the slab (Fig. 14a) which is likely to modify the state of the stress in the slab. In addition to the modified state of stress, it creates variations in slab curvature (Fig. 14d,e) which are argued (Bletery et al., 2016) to create heterogeneities in the strength of the interface resulting in more frequent ruptures.

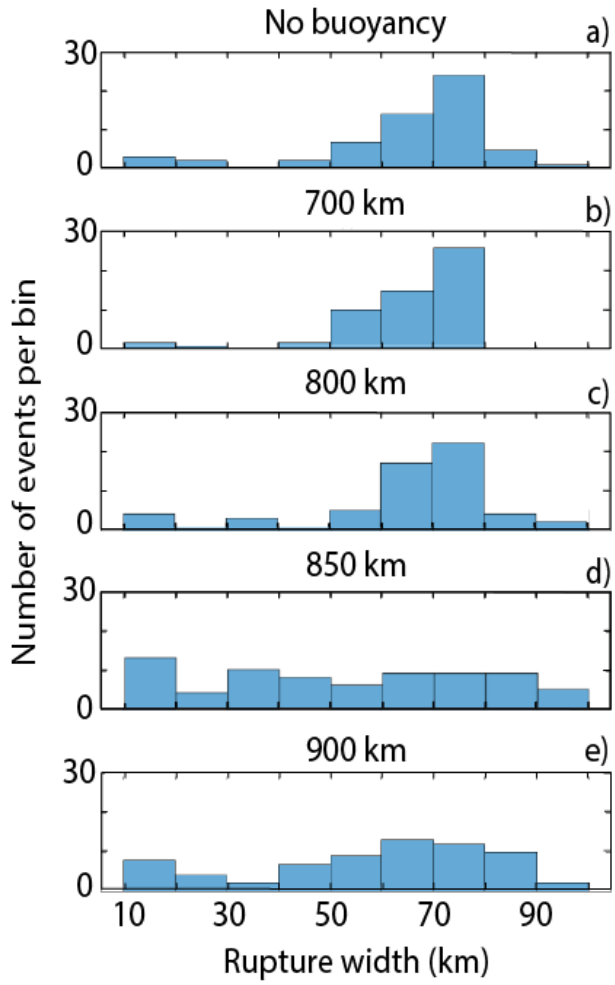

Figure 18: Rupture width distribution for varying initial lateral positions of the anomaly.

3.1.4. Size of the anomaly

I investigate the role of the size of the anomaly, since the anomaly dimensions in nature are uncertain. I study three sizes of the anomaly, i.e., 30.4 km in radius, 60 km in radius, and 90.5 km in radius. 30.4 km of radius represents half of the area of the 60-km radius anomaly, while 90.5 km represents twice the area of the 60-km radius anomaly.

a. Slab dip

Models do not predict any significant changes at the seismogenic zone neither for the slab dip nor for the slab curvature for different sizes of the anomaly (Fig. 19b,d). On the other hand, the geodynamic depths seem to be much more affected by the change in size, as suggested by the high R^2 of 0.838 for the slab dip and 0.697 for the slab curvature indicating significant correlations (Fig. 19c,e). The slab dip gets shallower, as the anomaly

gets larger, i.e., the dip changes from ~-30° (no buoyancy) to ~-22.5° (90.5 km of radius) (Fig. 19c). Also the slab curvature decreases one order of magnitude from ~0.12 (no buoyancy) to almost 0 (90.5 km of radius), i.e., a significant flattening of the slab with a larger buoyant anomaly (Fig. 19e). The size of the anomaly thus largely seems to matter at larger depths contrary to what is observed at the seismogenic zone.

The surface of contact between the anomaly and the slab is larger, which implies that the upward buoyancy force of the anomaly will be applied on a larger surface and at a higher rate since the buoyancy force ($F = \rho g V_d$ with F = the buoyancy force, ρ the anomaly in density, g the gravity force, and V_d the volume of the buoyant anomaly) is directly proportional to the volume leading to larger-scale changes in the slab, i.e., a shallower depth as well as a flattening of the slab. As observed at geodynamic depths, the tip of the slab is the most sensitive part of the slab to the buoyancy force, it was also the case for the density contrast and the initial distance from the trench (Fig. 9c, 14c).

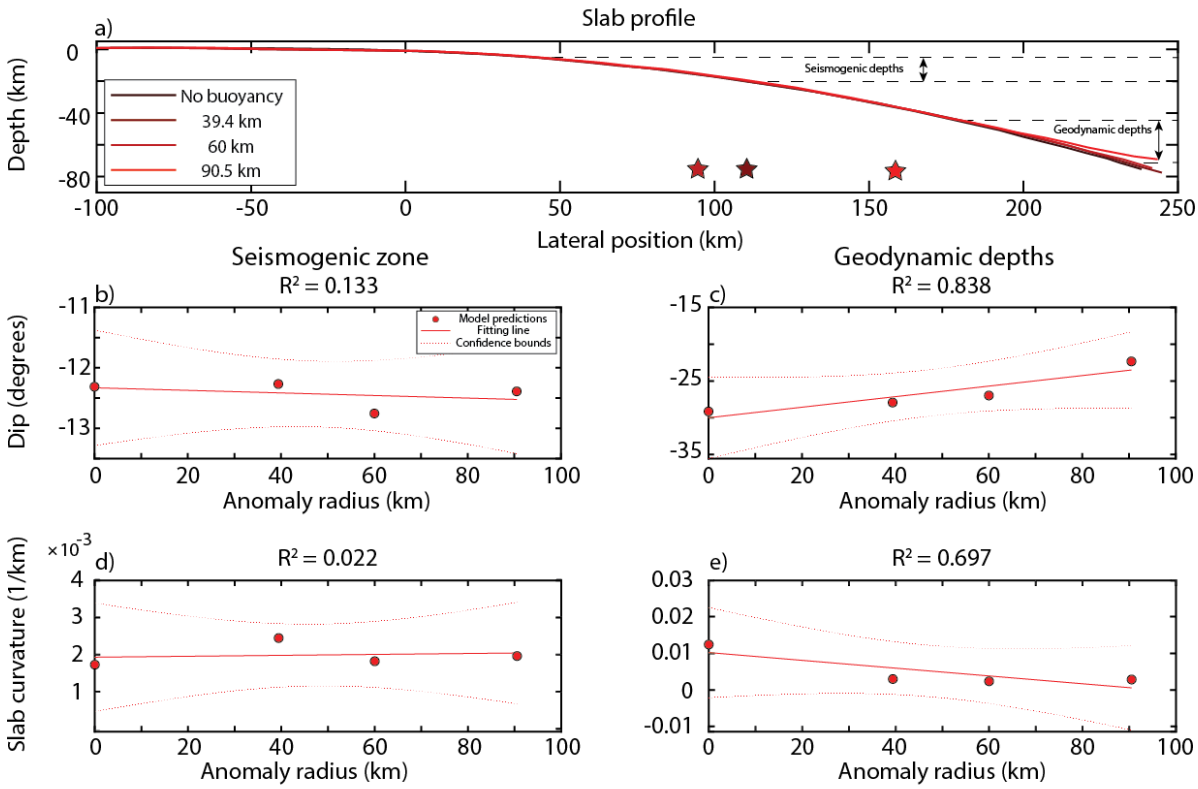

Figure 19: Slab profiles (a), slab dip (b-c) and apparent slab curvature (d-e) for different initial size of a density anomaly with an effective density contrast of 4.1 kg/m³ at t = 7.9 Myrs. (a) Stars indicate the horizontal center of the anomaly at the last timestep. The dashed lines delimit the seismogenic zone and the geodynamic depths areas of calculation of the slab dip and the slab curvature. (b-c) Seismogenic zone (b) and geodynamic depths (c). The less negative the value is, the shallower the slab dip is. (d-e) Seismogenic zone (d) and geodynamic depths (e). (b-e) The red dots are the model results, while the red lines are the linear regressions that fit the predictions best estimated using a root-mean-square (RMS) error method where $R^2 = 1$ is the best fit, the dashed lines are the 95% confidence bounds of the regression line. Slab curvature is calculated using circfit (Andrew Horchler (2022). Circfit (https://github.com/horchler/circfit), GitHub. Retrieved June 8, 2022) to extract the bending radius of the slab and obtain the slab curvature from 1/R where R is the bending radius (Turcotte and Schubert, 2012).

b. Topography

Models suggest that larger anomalies induce higher bulges in the forearc topography with an almost 600 m higher bulge as well as a 10 km displacement of the trench to the right (Fig. 20a,b). The changes in topography seem to correlate with the changes in geodynamic slab dip beyond 150 km from the trench but not in the same proportions. As a matter of fact, the ~600-m high in the topography corresponds to a ~1 km shallower slab (Fig. 20b,d). The changes observed in topography seem to be about half of those obtained in the slab depth. However, after 200 km from the trench, the slab keeps getting shallower while the topography returns to the altitudes similar to the reference model topography (Fig. 20b,d).

A larger anomaly applying its buoyant force over a larger area (see 3.1.3.a) makes the slab rise more and displaces the trench towards the continent, which creates more pressure at the deformation front in the overriding plate and, therefore, more deformation. Further away from the trench, below the continental plate, a contribution to the topography can be attributed to the uplift of the slab at depth but part of the force created by its upward force is absorbed by either the elasticity of the lithosphere or the non-elastic behavior of the lower crust (see 3.1.2a)

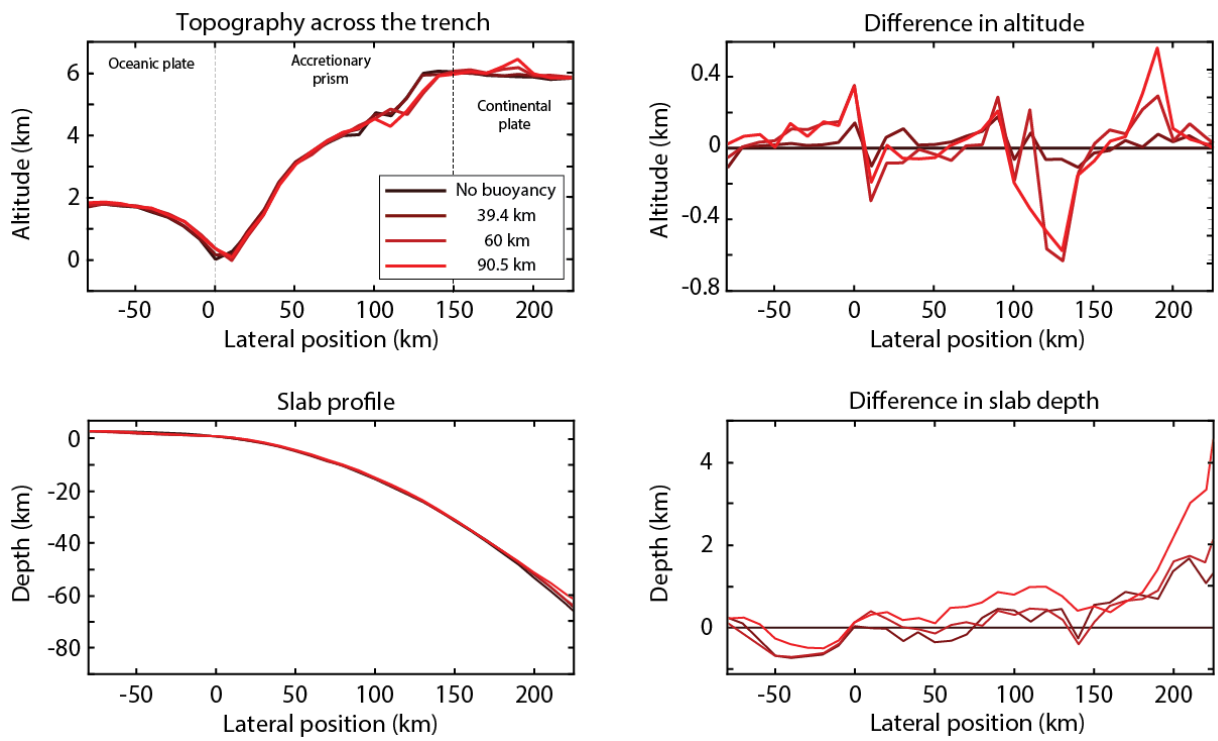

Figure 20: Topography (a-b) and slab profiles (c-d) for varying radii of the sub-slab density anomaly from the left boundary for an effective density contrast of 4.1 kg/m^3 at t = 7.9 Myrs. (a) Altitude with respect to the trench at the isostatic equilibrium. (b) Changes in topography. (c) Slab profiles. (d) Variations in vertical position of the slab.

c. Earthquakes sequences

Interseismic coupling

With a larger anomaly, models predict a decrease in the upper plate velocity towards the land, i.e., the same direction as the subducting slab, in the updip region (~ 100 km) while a slight increase in these velocities at the downdip region (~ 140 km) is observed (Fig. 21a,b). Also, the larger anomalies seem to allow for a more heterogeneous nucleation and extent of the seismogenic zone while for smaller anomalies, the hypocenter locations seem to be centered around 120 km from the trench with a relatively constant extent of the seismogenic zone (Fig. 21a,b).

The interseismic coupling confirms the velocity observations because, in the updip region (before 60 km from the trench), the coupling is lower the larger the anomaly is (Fig. 21c). Beyond 70 km from the trench until the downdip region, the interseismic coupling becomes significantly higher for the largest anomaly than for the others (no buoyancy, 39.4 km, and 60 km) (Fig. 21c).

Analyzing the velocities on both sides of the megathrust and the resulting coupling of the plates, the results suggest that, the larger the anomaly is, the less coupled the plates are at the updip limit of the siesmogenic zone, and the more coupled they are at the downdip limit.

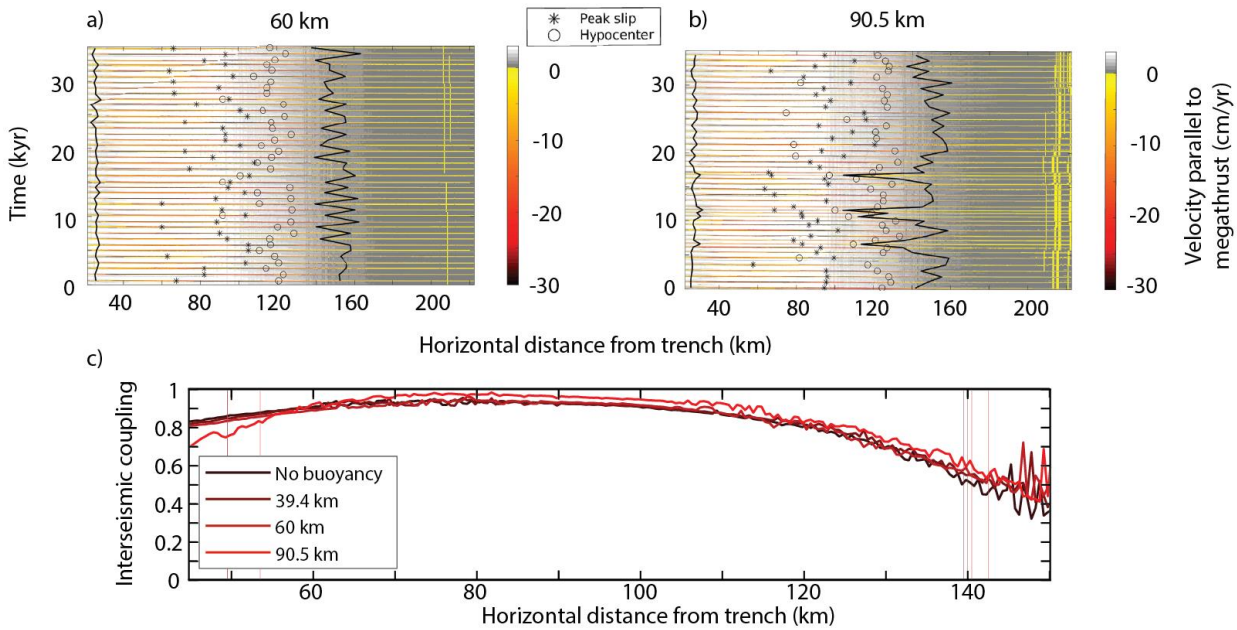

Figure 21: Velocity parallel to the megathrust (a-b) and interseismic coupling (c). (a-b) Velocity parallel 6.4 km above the megathrust (overriding plate) for the reference model (a) and 4.1 kg/m^3 of effective density contrasts (b). Velocities are positive (gray-white) towards the continent. Continuous black lines are the limits of the ruptures for each event. Circles are hypocenter locations and starts are the peak slip locations. (c) Interseismic coupling for different density contrasts. Calculated by the ratio of velocities at 6.4 km above and below the megathrust, 1 is the theoretical value for two fully coupled plates. The vertical lines are the up- and downdip limits of the seismogenic zone based on the 150 and 350°C isotherms.

In the updip region, for a larger anomaly, the lower velocities of the overriding plate towards the land and the lower coupling correlate with slightly higher values of plastic strain rates with respect to a smaller anomaly (Fig. 23b,d). In the downdip region, the higher velocities towards the continent correspond with a shorter extent of high viscous strain rates and slightly lower values than for a smaller anomaly (Fig. 22f,h).

Higher visco-plastic strain rates indicate that the megathrust tends to creep more (i.e., lock less) in the updip region while it is lower in the downdip. Also, higher velocities towards the continent reflect a higher coupling between the overriding plate and the subducting slab. Therefore, here one can argue that, at the updip limit of the subduction zone, the two plates tend to creep more when the buoyant anomaly is larger while they tend to be more coupled at the downdip limit. (see 3.1.2.c)

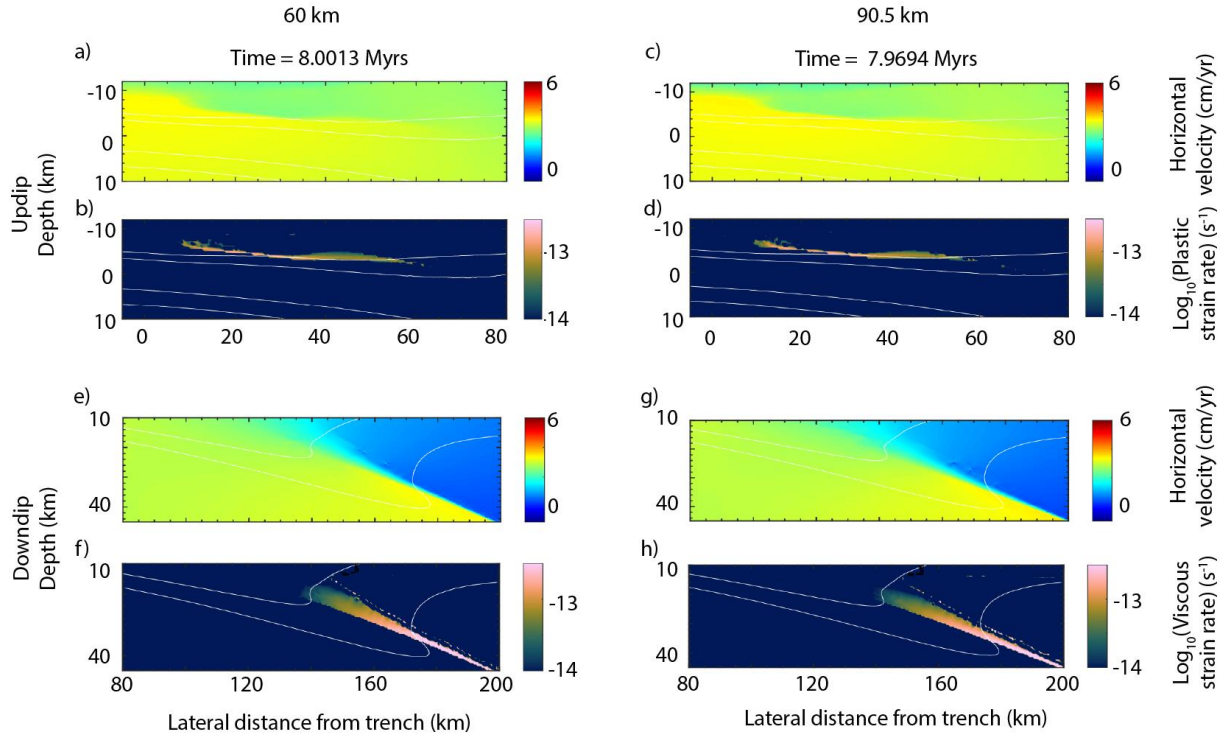

Figure 22: Visco-plastic strain rates at the megathrust for different initial radii of the sub-slab buoyant anomaly with an effective density contrast of 4.1 kg/m^3. (a-d) Snapshot of horizontal velocity (a-b) and plastic strain rate (lower c-d) in the updip region. The plastic strain rates are displayed in a log scale. The white lines indicate the 100°C, 150°C, 350°C, and 450°C isotherms. (e-h) Snapshot of horizontal velocity (e-f panel) and plastic strain rate (g-h) in the downdip region. The white lines indicate the 350°C and 450°C isotherms. (a, c, e, g) Reference model. (b, d, f, h) Buoyancy model with 26.9 kg/m^3 of effective density contrast.

Rupture widths

Larger anomalies tend to make megathrust interfaces rupture more frequently and the extent of their ruptures more heterogeneous (Fig. 23). One can find most of the rupture widths around the 60-80-km bins for smaller anomalies, while there are more events detected for larger anomalies and the ruptures tend to be distributed around both the 10-20-km bin and the 60-80-km bins in a bimodal distribution (Fig. 23).

With a larger anomaly, the seismicity becomes more frequent and the rupture widths tend to be more evenly distributed with a significant increase in narrow ruptures. Larger anomalies like closer anomalies induce an unbending of the slab at depth, therefore, a secondary hinge in the slab which may be suspected to change the state of stress as described in 3.1.3.c.

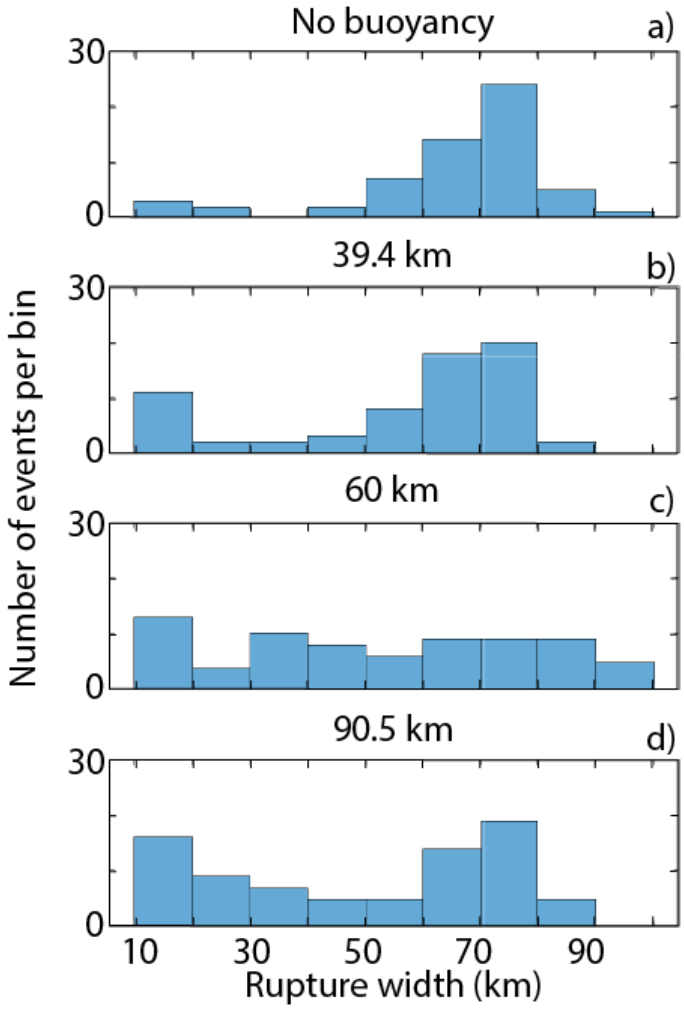

Figure 23: Rupture width distribution for varying initial radii of the anomaly.

In summary, I have shown that the presence of a sub-slab buoyancy causes changes in both the subduction geometry, the seismicity, and the interseismic coupling with:

- A higher density contrast between the mantle and the asthenospheric anomaly produces at most an uplift of 700 m in the topography for an effective density contrast of 42.9 kg/m^3 as well as a 2°-steeper slab dip at the seismogenic zone (4-20 km depth), but a 5°-shallower slab dip at geodynamic depths (> 45 km depth). It creates a bimodal distribution of the rupture widths between narrow (10-20 km) and relatively large (60-80 km) ruptures. The ruptures are also more frequent with almost 20 more events recorded for 42.9 kg/m^3 of effective density contrast than for the reference model. Higher density contrasts induce a lower interseismic coupling near the updip region and increases it closer to the downdip region due to the buoyancy force applied.
- A buoyant anomaly with a 4.1 kg/m^3 of effective density contrast that is initially located closer to the trench induces higher forearc topography gets higher. It produces at most a bulge that is 450 m-high when it is located below the subduction zone from the beginning of the model. The closer the anomaly is to the trench from the beginning, the more flattening it will induce to the tip of the slab when it reaches geodynamic depths. As a matter of fact, the tip of the slab undergoes a shallowing of almost 10 degrees almost doubling the slab curvature with respect to the model where the anomaly is the furthest away from the trench. At the seismogenic zone, the effects are much more moderate and only

reduces the slab curvature without significantly affecting the slab dip. The closer the anomaly is located to the trench, the more frequent the seismicity with a more even distribution of its rupture width with 20 more events detected in the model where the anomaly is the closest to the trench from the beginning. It also induces a decrease in the coupling in the updip region but an increase closer to the downdip limit.

- A large buoyant anomaly, within the range tested, can produce up to 600 m of uplift in the forearc topography. In terms of geometry, increasing the size of the anomaly does not impact in any observable way the slab dip at the seismogenic zone, but it tends to make the slab flatten at geodynamic depths where the slab dip is almost 10 degrees shallower and a slab curvature that tends to 0. It induces more frequent seismicity with 10 more events recorded for the largest anomaly than for the smallest anomaly. It also produces narrower rupture widths. The interseismic coupling between the two plates is lower at the updip limit of the seismogenic zone when the anomaly is larger but the coupling is higher at the downdip limit.
- The depth of the anomaly was also varied but did not show any significant change in any of the variables monitored (see Appendix).

3.2. Plate age variations

3.2.1. Slab dip

Simulation results indicate that the younger the slab, the steeper the slab dip is at the seismogenic zone with a steepening of ~5° between a slab of 100 Ma and a slab of 7.5 Ma (Fig. 24b). This trend seems to continue at geodynamic depths (~100-150 km), but it is weaker as the decrease of 0.5 in R^2 indicates (Fig. 24c). One can also note that older slabs tend to have a more constant slab dip over different depths (Fig. 24a). One could argue that a slight increase may be observed in the slab curvature at geodynamic depths from young to old slabs, but this is not highlighted by the regression line due to the presence of an outlier at 11 Ma.

These model results agree with those of Dasdgupta et al. (2021) who did see that old slabs have a relatively constant trajectory when sinking into the mantle with respect to younger slabs. From this, they showed that old slabs which are also dense and thick tend to have a lower curvature and argue that the higher stiffness (i.e., higher viscosity) of old slabs increases the resistive bending moment. At the seismogenic zone, density resulting from temperature of the slab is the main control on slab dip. An older, colder, and therefore, denser slab, sinks more easily into the mantle, i.e., closer to the left boundary (Fig. 24a). Once the subduction process is in place, however, the main control is the stiffness of the plate because a denser and thicker plate tends to resist more to bending due to its thickness, it does not sink as steeply as a weak and thin plate would (Dasdgupta et al. (2021)).

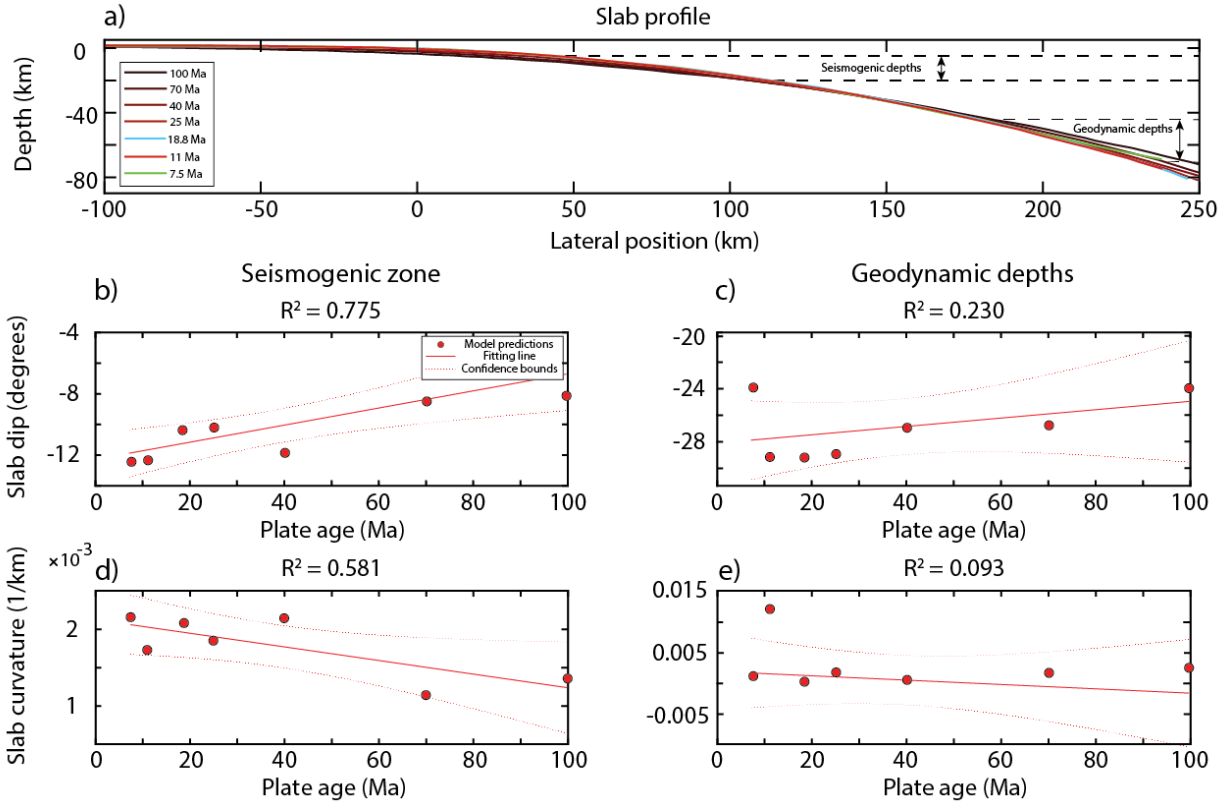

Figure 24: Slab profiles (a), slab dip (b-c) and apparent slab curvature (d-e) for different oceanic slab ages at t = 7.9 Myrs. (a) Stars indicate the horizontal center of the anomaly at the last timestep. The dashed lines delimit the seismogenic zone and the geodynamic depths areas of calculation of the slab dip and the slab curvature. (b-c) Seismogenic zone (b) and geodynamic depths (c). The less negative the value is, the shallower the slab dip is. (d-e) Seismogenic zone (d) and geodynamic depths (e). (b-e) The red dots are the model results, while the red lines are the linear regressions that fit the predictions best estimated using a root-mean-square (RMS) error method where $R^2 = 1$ is the best fit, the dashed lines are the 95% confidence bounds of the regression line. Slab curvature is calculated using circfit (Andrew Horchler (2022). Circfit (https://github.com/horchler/circfit), GitHub. Retrieved June 8, 2022) to extract the bending radius of the slab and obtain the slab curvature from 1/R where R is the bending radius (Turcotte and Schubert, 2012).

3.2.2. Topography

The models predict that when the slab is younger, the continental lithosphere tends to build a higher fore-arc topography in particular at the transition between the accretionary prism and the continental lithosphere where one can see a difference of 2.75 km between the oldest slab model and the youngest (Fig. 25a,b). Differences are not as sharp but still significant on the continental plate where the forearc tends to lie 500 m higher for the youngest slab model than for the oldest (Fig. 25a,b). Variations are also observed in the altitude of the seafloor that tends to be 3 km higher for the youngest plate with respect to the oldest (lithostatic equilibrium) 50 km before the reference trench location (Fig. 25a,b). Here, changes in slab depth correlate with the altitude of the slab and the accretionary prism only up to 100 km from the trench but not with the overriding plate (Fig. 25b,d).

These simulation results agree with natural subduction zones where the seafloor tends to lie lower in subduction zones where the oceanic slab is old (e.g., Mariana Trench) and higher with young oceanic slabs (e.g., Cascadia). Isostatic equilibrium implies that a compensation depth exists where the lithostatic pressure is equal for different rock columns. The lithostatic pressure is defined by $P = \rho \times g \times h$, where P is the lithostatic pressure, ρ the density, g is the acceleration of gravity, and h the height of the rock column. In the

oceanic plate, the density decreases from a younger to an older slab, so the topography must increase to reach the isostatic equilibrium resulting in a seafloor that lies higher for a younger slab. Meanwhile, the continental lithosphere always has the same thickness and geotherm at the initial stage so any variations must be explained by changes in the oceanic lithosphere. Consequently, a younger, therefore higher, slab induces higher topography because it tends to push the continental lithosphere up more than an easily sinking old slab. This has also been observed in simulations by van Dinther et al. (2010).

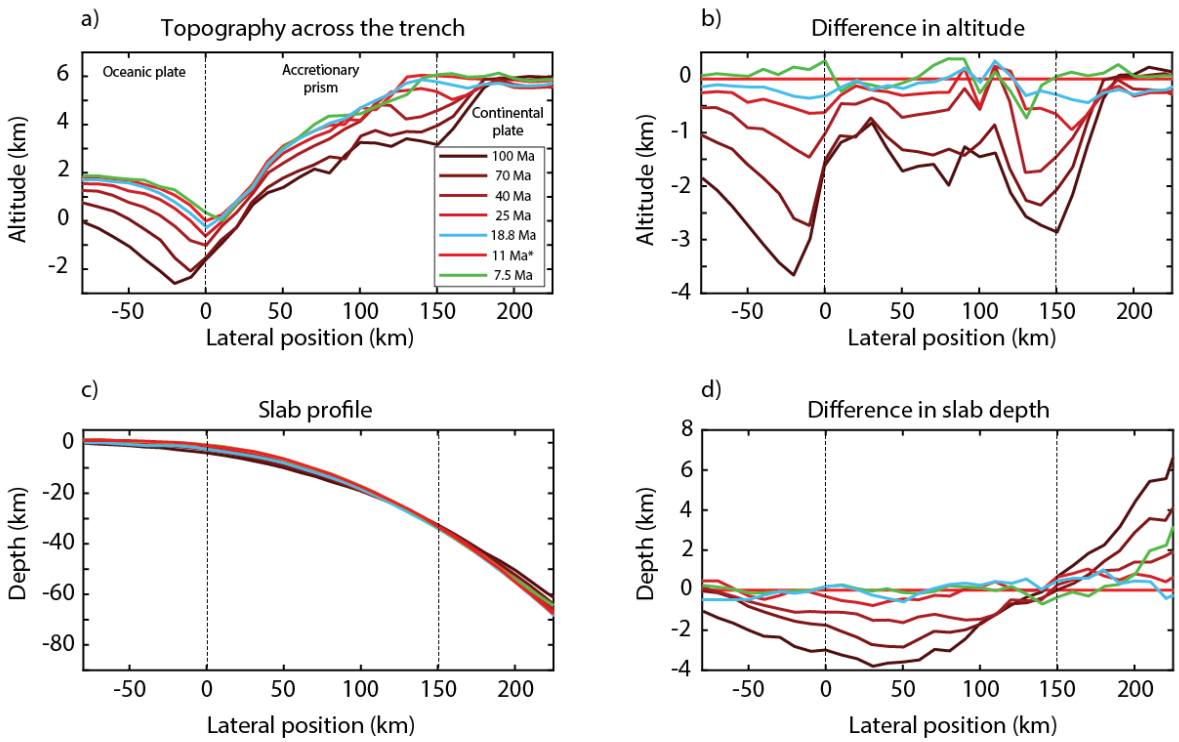

Figure 25: Topography (a-b) and slab profiles (c-d) for varying oceanic slab ages. (a) Altitude with respect to the trench at the isostatic equilibrium. The star indicates the reference model (11 Ma). (b) Changes in topography with respect to the reference model. (c) Slab profiles. (d) Variations in vertical position of the slab with respect the reference model.

3.2.3. Earthquake sequences

Interseismic coupling and rupture widths

Overall, interseismic velocities in the overriding plate of old slabs go at higher rate towards the continent than that of young slabs (Fig. 26a,b). Only between 130 and 140 km from the trench, lower rates are observed for the older slab (Fig. 26a). When comparing directly the interseismic coupling of the different models, one can observe that all along the megathrust, old slabs are more coupled to the overriding plate than young slabs are (Fig. 26c). The ratio increases of 0.1 in the updip region from the youngest slab, 7.5 Ma, to the oldest slab, 100 Ma. One can also notice that the coupling drop towards very low value (0 eventually) much slower for old slabs than for young slabs whose coupling at 140 km from the trench is 0.3 while that of old slab is still 0.9 (Fig. 26c).

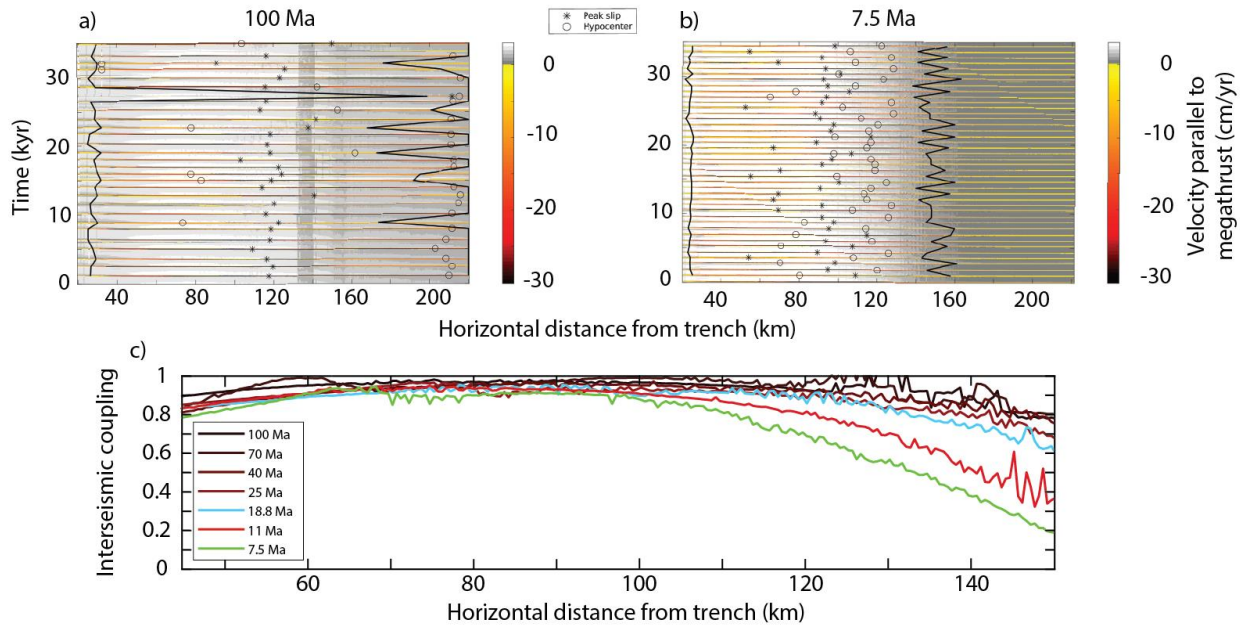

Figure 26: Velocity parallel to the megathrust (a-b) and interseismic coupling (c). (a-b) Velocity parallel 6.4 km above the megathrust (overriding plate) for the reference model (a) and 4.1 kg/m^3 of effective density contrasts (b). Velocities are positive (gray-white) towards the continent. Continuous black lines are the limits of the ruptures for each event. Circles are hypocenter locations and starts are the peak slip locations. (c) Interseismic coupling for different density contrasts. Calculated by the ratio of velocities at 6.4 km above and below the megathrust, 1 is the theoretical value for two fully coupled plates. The vertical lines are the up- and downdip limits of the seismogenic zone based on the 150 and 350ºC isotherms.

Overall, the younger a slab is, the least coupled it is to the overriding plate. This is also confirmed in the updip region where the younger slabs have a slightly narrower zone of plastic behavior but the values are significantly higher than those of older slabs (Fig. 27g,h) indicating that creep is more important at the interface between a younger oceanic plate and the overriding plate than an older oceanic plate. Younger slabs are hotter and lead to higher temperatures across the megathrust interface (Fig. 27c,d). Higher temperatures at similar depths lead to lower viscositie, such that the brittle-ductile transition occurs at shallower depths already. This limits the width of the region of interseismic coupling significantly at larger depths.

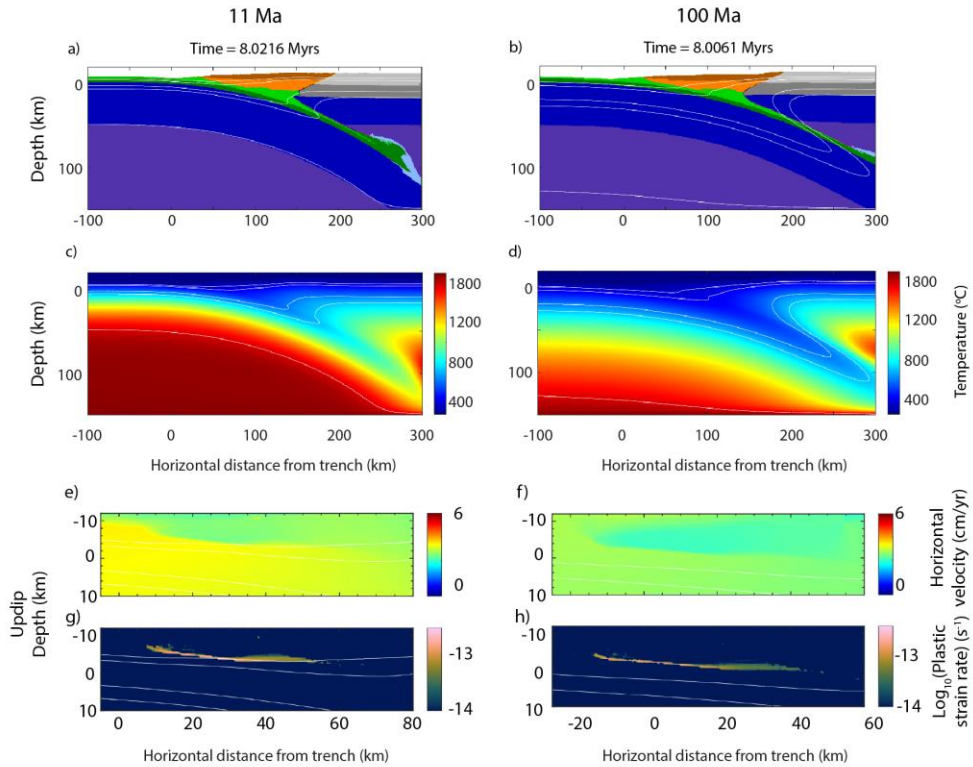

Figure 27: Rock composition (a-b), temperature (c-d), and plastic strain rates at the megathrust for different oceanic slab ages. (a-b) Rock composition at 8.0 Myrs for an 11 Ma oceanic slab (reference model) (a) and a 100 Ma oceanic slab (b). (c-d) Temperature. (e-h) Snapshot of horizontal velocity (e-f) and plastic strain rate (g-h) in the updip region. The plastic strain rates are displayed in a log scale. The white lines indicate the 100°C, 150°C, 350°C, and 450°C isotherms.

Here, it is clear that the younger an oceanic plate is, the narrower the extent of the seismogenic zone is, and the shorter the recurrence interval is leading to higher rates of seismicity (Fig. 26a,b and 28). One can also notice that the seismic events tend to nucleate much deeper for older slabs, i.e., ~200 km from the trench for older slabs and ~120 km for the youngest (Fig. 26a,b). Older slabs tend to have relatively evenly distributed rupture widths ranging between 10 and 100 kms while younger slabs tend to have significantly more frequent seismicity and with ruptures distributed over a narrower range between 10 and 70-80 km (Fig. 28).

Here, the first-order factor controlling the rupture is the slab dip. As a matter of fact, Muldashev & Sobolev (2020) argue that shallower the slab dips, the wider the seismogenic zone is and, consequently, the larger the further the ruptures may propagate. Generally, it is the oldest slabs that show the shallower slab dips at the seismogenic zone (Fig. 24b) and the widest seismogenic zone (Fig. 26a,c) which explains why they tend to host larger and less frequent ruptures (Fig. 28). Also, Heuret et al. (2011) show that temperature plays an important role on the width of ruptures where rupture width decreases the younger the plate is because, for older and colder slabs, the frictional properties tend to persist at depth while they do not for younger, hotter slabs.

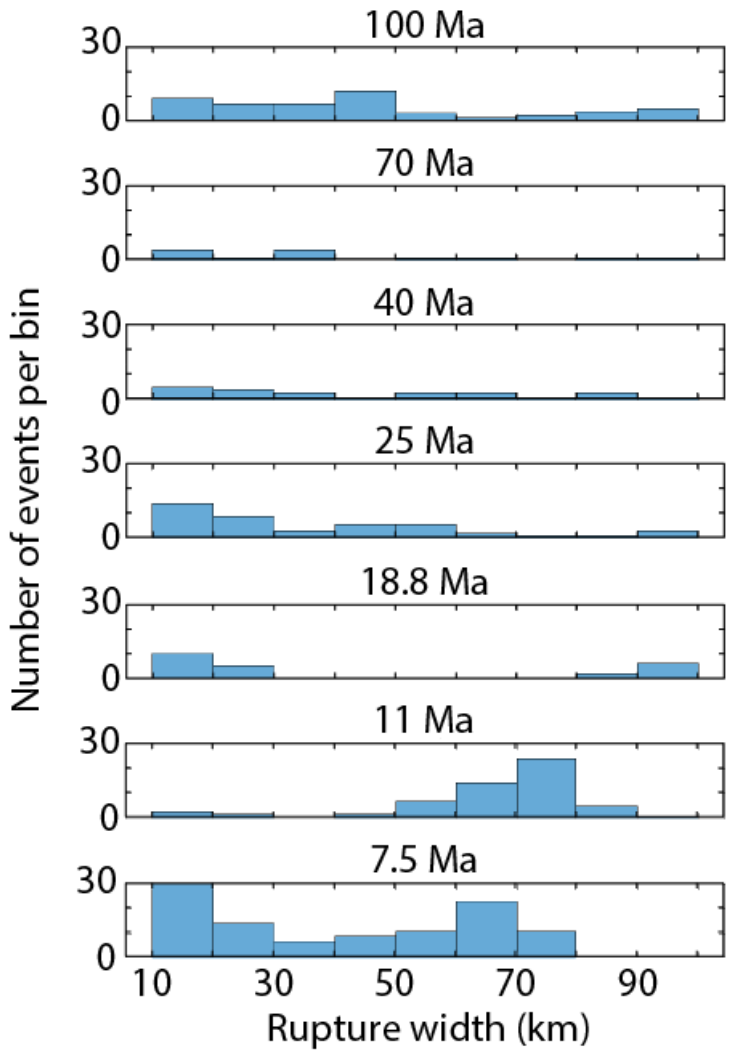

Figure 28: Rupture width distribution for varying plate ages.

In summary, for the different observables highlighted here, I notice that temperature seems to have an important control on the subduction zone's morphology, dynamics, and seismicity. When slabs are older, they are also colder, therefore stiffer, so they tend to dip shallower into the mantle and in a more constant trajectory than that of younger slabs. Nevertheless, as it is more difficult for younger slabs to sink into the mantle, they tend to push more onto the overriding plate forming higher topography. Younger slabs, due to their temperature and steep slab dip, tend to have narrower seismogenic zone leading to narrower ruptures and interseismic coupling.

4. Discussion

4.1. Cascadia

Here, I have shown the effects of plate age variations and sub-slab buoyancy on the the geometry of the subduction zone, the topography, the interseismic coupling, and the seismicity and observed that the density contrast produced by the anomaly, its size, and the temperature field resulting from the cooling of the plate are the factors controlling the most the different aspects of the subduction zone in both long- and short-term effects. To be able to rank their importance in the context of the Cascadia Subduction Zone (CSZ), I extrapolate and compare their impact on the observed values.

Kelsey et al. (1994) proposed that along-strike plate age variations can explain the lateral segmentation of the CSZ. However, my results show that variations in plate age from 7.5 Ma and 18 Ma (Fig. 24 and 25) cannot solely explain the geometry variations observed between the different segments (section 3.2) but only half of them. My models predict a 2-degree shallowing of the slab dip for a slab of 18.8 Ma (Central Cascadia) with respect to a slab of 7.5 Ma (Southern Cascadia) at the seismogenic zone (Fig. 24) while observations show a shallowing of the slab dip in Northern and Southern Cascadia and a steepening in Central Cascadia (McCrory et al., 2012). Therefore, the models suggest an opposite behavior of the slab dip with respect to the natural observations at the seismogenic zone. The forearc topography changes at most of ~500 m between the 18.8 Ma slab and the 7.5 Ma slab (Fig. 25) while the observed forearc topography is ~1 km higher in the Northern and Southern segments than it is in the Central segment (Bodmer et al., (2018; 2020)). When the plate is younger, seismicity is also more frequent (Fig. 26 and 28) which agrees with the observations made by Brudzinski and Allen (2007). In the CSZ, lower interseismic coupling is observed in Central Cascadia Schmalzle et al. (2014) where the plate is older which is opposite to what I simulated where I see that the older the plate, the higher the interseismic coupling is (Fig. 26).

On the other hand, Bodmer et al., (2018; 2020), based on a more recent plate age model of the CSZ by Wilson (2002), proposed that two independent mantle upwellings in Northern and Southern Cascadia push the slab upward resulting in a lateral segmentation and plate age variations can be neglected. The density contrast inferred by the observations is in the order of 5 kg/m^3, therefore, we used a reference anomaly of 4.1 kg/m^3 of effective anomaly to simulate accurately the conceptual model proposed. Based on our simulations, a sub-slab buoyant asthenosphere alone cannot explain the full lateral segmentation of the subduction zone but only half of it. First, the slab dip induced by an effective density contrast of 4.1 kg/m^3 steepens of ~0.5 degree at the seismogenic zone (Fig. 9) which does not agree with the observations that show a 2-degree shallowing of the slab dip in the segments affected by the sub-slab anomaly (McCrory et al., 2012). In terms of forearc topography, for an effective density contrast of 4.1 kg/m^3, the models show an uplift of only 300 m with respect to the reference model without buoyancy (Fig. 10) while the uplift observed in Northern and Southern Cascadia is in the order of ~1 km (Bodmer et al., (2018; 2020)). To match the topography change observed in Cascadia, the anomaly needs to be larger. The 60-km radius anomaly used as a reference model represents an area of 9,048 km^2 and, by extrapolating the results on the size of the anomaly, one can predict that the area needed to match a ~1 km bulge in the topography is ~31,000 km^2 (Fig. 10). This area can be modeled by using a 70-km radius anomaly that represents a full disk contrary to my models where the anomaly is not a full circle. This agrees with nature where Bodmer et al., (2018; 2020) imaged the anomalies between 100 and 250 km corresponding to a 75-km radius anomaly. On the short-term changes, the pattern described by the interseismic coupling is more difficult to compare because the introduction of a sub-slab buoyancy induces a decrease in the interseismic coupling in the updip region but an increase in the interseismic coupling in the downdip region (Fig. , and observations have shown that interseismic coupling increases in Northern and Southern Cascadia where the anomalies are located (Schmalzle et al. (2014)). So, observations fit my simulations in the downdip region but not in the updip. On the the other hand, simulations show that seismicity increases and ruptures are narrower when the anomaly is present which agrees with the observations (Schmalzle et al. (2014)).

In reality, a combination of both sub-slab buoyancy and plate age variations may be taking place in the CSZ. My results show a 500-m uplift in Southern Cascadia for an age of 7.5 Ma (Kelsey et al. (1996)) compared to a slab of 18.8 Ma corresponding to Central Cascadia. Therefore, to find the same topography change as observed in nature, one must introduce a sub-slab buoyancy affecting the subduction zone as much as the plate age variations do. This would correspond to an uplift of ~500 m as well which, based on our reference setup and interpolation would be an ~80-km radius anomaly (Fig. 20).

With varying density contrasts, my simulations, even for the highest density contrasts, do not predict as large changes in the slab geometry as those simulated by Betts et al. (2012) who studied the effect of a strong mantle plume below the slab of 50 kg/m^3 and 100 kg/m^3 of density contrasts. I suspect that two factors play an important role here: elasticity of the plates and the presence of the overriding plate. Here, elasticity of both the subducting and overriding plate lithosphere ensures an internal strength that absorbs stresses applied to their bottom and redistributes them over a larger area. This is similar to what happens when one accounts for regional isostasy (flexure) instead of local isostasy. Overall, the more realistic rheological layering in my models likely portrays a more realistic impact of variable density contrasts.

4.2. Model Limitations and Future Work

Here, I simulate a Cascadia-like subduction zone, but direct comparison with the natural subduction zone can be challenging due to modeling simplifications. Geological heterogeneities in the continental plate are not accounted for such as the Siletzia terrane present in Northern and Central Cascadia (Fig. 1). Furthermore, I use the half-space cooling model to build the initial temperature field but, as argued by previous studies, the Juan de Fuca Plate does not seem to be consistent with the half space cooling model (Bell et al., 2016; Byrnes et al., 2017; Eilon and Abers, 2017). Therefore, my initial temperature field might be different from the actual structure of the Juan de Fuca Plate, especially considering that I apply a constant slab age throughout the plate.

Also, in reality, the subduction zone is a combination of the three segments that may be dependent on one another and where material can move in any direction. For example, toroidal flow at the slab edge in Southern Cascadia has been inferred (Long, 2016), oblique subduction (McCaffrey et al., 2000), or the complex structure of the Juan de Fuca system which is formed by three semi-independent plates, separated by important fault zones, that affect the subduction dynamics (DiPietro, 2018). The 2-D model transect across the trench does not allow to investigate such processes, but it is a very useful tool to isolate each parameter, study their effect independently, and make general interpretations that may be applied to other subduction zones. Contrary to nature, a 2-D plane strain numerical model actually produces forces and stresses of a density anomaly that extends inifinitely along-strike. Therefore, I may overestimate the size of some effects of the sub-slab buoyancy. Also, I model a sub-slab buoyancy that is located under the slab directly during subduction initiation, however, Bodmer et al. (2018; 2020) argue that the sub-slab anomaly has entered the subduction zone when it was already in place so the effects of the sub-slab buoyancy on the long-term changes (i.e., topography and slab dip) may be overestimated.

I was not able to make models with large variations in depth because this would imply building a larger model and would require even larger computing resources. Hence, I extrapolated the size of the anomaly to infer that a 70-km radius anomaly would be a good estimate for Cascadia which seems reasonable given the clear correlation (R^2 = 0.981). The duration of coseismic events is much longer (> 50 years) than that of natural events (~ a few seconds to minutes) and will need to be improved in future modeling work. However, studies in strike-slip faults comparing such rate-dependent friction slip transients to dynamic earthquakes generated with rate-and-state friction suggests differences in recurrence interval and amount of slip less than about 20% (Preuss, PhD thesis ETHZ, 2020). Such changes are not expected to impact our comparisons on the impact of these parameters in subduction zones.

In the future, the understanding of the CSZ could be improved by building a model tracing a more realistic history of the anomaly from the initiation of Cascadia to the arrival of the anomaly below the seismogenic zon. Also, 3-D models of the CSZ would be useful to understand the interactions between the different segments and the sub-slab region. In longer models, do the mantle upwellings only stay below their own segments or would they be able to diffuse into the other segments on the long-term?

5. Conclusion

I use seismo-thermo-mechanical models tuned to Cascadia to compare the impact of a sub-slab density anomaly to that of slab age variations for the geometry, seismicity, and interseismic coupling characteristics of the subduction zone. The models predict that the slab dip tends to steepen at the seismogenic zone and shallows at geodynamic depths for increasing density contrasts. The shallowing in slab dip correlates with higher forearc topography implying that the buoyancy force induced by the sub-slab anomaly induces changes in both the slab and the overriding plate. The presence of the density anomaly also decreases the interseismic coupling by reducing the amount of brittle behavior in favor of creep along the megathrust in the updip region while in the downdip region, it is the brittle behavior that dominates and allows for higher coupling between the two plates. The presence of the anomaly increases the frequence of seismicity and reduces the size of the ruptures because of its impact on the geometry of the slab.

I also find that younger slabs tend to dip more steeply at the seismogenic zone into the mantle due to their reduced elastic stiffness. However, they do induce higher bulges in the forearc topography by pushing more onto the overriding plate, because their buoyancy makes it more difficult for them to sink into the mantle. This means that isostasy is more important than slab dynamics and stiffness for overriding plate topography. Because younger plates are warmer, the megathrust becomes warmer reducing the viscosity awhich results in lower coupling. This also influences the seismicity of younger slabs which happens more frequently but over narrower extents because of their seismogenic zone that is narrower due to a higher temperature at the megathrust and a steeper slab dip.

Based on the simulations presented here and the magnitude of changes of the slab dip, topography, interseismic coupling, and seismicity observed in nature, the plate age variations observed by Kelsey et al. (1994) can explain the seismicity pattern, half of variations in topography and does not agree with our slab dip and interseismic coupling results. On the other hand, our reference sub-slab buoyancy model can explain the seismicity pattern as well as the downdip interseimsic coupling, the third of the topography changes, but it does not agree with our slab dip results at the seismogenic zone.

Extrapolating to the size of the observed anomaly, I predict changes in topography of 1 km without change of the slab dip at the seismogenic zone but a shallowing of 12 degrees at geodynamic depths, lower interseismic coupling at the updip limit of the seismogenic zone while higher interseismic coupling at the downdip limit and higher and more heterogeneous seimsicity. This means that along-strike topography, seismicity and downdip interseismic coupling variations in Cascadia can be explained without variations in slab age. Hence, the hypothesis explaining lateral segmentation in Cascadia by sub-slab density anomalies as proposed by Bodmer et al. (2018; 2020) is physically viable and the simplest solution implying least variations along-strike.

6. Acknowledgments

Thank you to both of my supervisors Dr. Ylona van Dinther and Dr. Miles Bodmer who invited me to work on this project, pushed me to challenge myself to acquire new skills and further knowledge, and helped me start my career. Thank you to Maaike Fonteijn for her work on the output of the Event Picking Algorithm and accepting to answer my numerous questions. Thank you to Prof. Emilie Hooft and Prof. Douglas Toomey for their constructive discussions on Cascadia. Finally, special thanks to everyone who supported me mentally and made me have a good time during lunch breaks: Sjaak, Maaike, Mhina, Eva, Daan, Jasper, Antoine, Nemanja, Meng, Noortje, Job, and Vincent. The eejit High Performance Cluster (HPC) of Utrecht University is used to carry out this study.

7. References

Bletery, Q., Thomas, A. M., Rempel, A. W., Karlstrom, L., Sladen, A., & De Barros, L. (2016). Mega-earthquakes rupture flat megathrusts. Science, 354(6315), 1027-1031.

Bell, S., Ruan, Y., and Forsyth, D. W. (2016), Ridge asymmetry and deep aqueous alteration at the trench observed from Rayleigh wave tomography of the Juan de Fuca plate, J. Geophys. Res. Solid Earth, 121, 7298– 7321, doi:10.1002/2016JB012990.

Betts, P. G., Mason, W. G., & Moresi, L. (2012). The influence of a mantle plume head on the dynamics of a retreating subduction zone. Geology, 40(8), 739-742.

Blaser, L., Krüger, F., Ohrnberger, M., & Scherbaum, F. (2010). Scaling relations of earthquake source parameter estimates with special focus on subduction environment. Bulletin of the Seismological Society of America, 100(6), 2914-2926.

Bodmer, M., Toomey, D. R., Hooft, E. E., & Schmandt, B. (2018). Buoyant asthenosphere beneath Cascadia influences megathrust segmentation. Geophysical Research Letters, 45(14), 6954-6962.

Bodmer, M., Toomey, D. R., Roering, J. J., & Karlstrom, L. (2020). Asthenospheric buoyancy and the origin of high-relief topography along the Cascadia forearc. Earth and Planetary Science Letters, 531, 115965.

Braun, J. (2010). The many surface expressions of mantle dynamics. Nature Geoscience, 3(12), 825-833.

Brizzi, S., Becker, T. W., Faccenna, C., Behr, W., van Zelst, I., Dal Zilio, L., & van Dinther, Y. (2021). The role of sediment accretion and buoyancy on subduction dynamics and geometry. Geophysical Research Letters, 48(20), e2021GL096266.

Brudzinski, M. R., & Allen, R. M. (2007). Segmentation in episodic tremor and slip all along Cascadia. Geology, 35(10), 907-910.

Byrnes, J. S., Toomey, D. R., Hooft, E. E., Nábělek, J., & Braunmiller, J. (2017). Mantle dynamics beneath the discrete and diffuse plate boundaries of the J uan de F uca plate: Results from C ascadia I nitiative body wave tomography. Geochemistry, Geophysics, Geosystems, 18(8), 2906-2929.

Chen, C., Zhao, D., & Wu, S. (2015). Tomographic imaging of the Cascadia subduction zone: Constraints on the Juan de Fuca slab. Tectonophysics, 647, 73-88.

Crameri, F., Schmeling, H., Golabek, G. J., Duretz, T., Orendt, R., Buiter, S. J. H., ... & Tackley, P. J. (2012). A comparison of numerical surface topography calculations in geodynamic modelling: an evaluation of the 'sticky air'method. Geophysical Journal International, 189(1), 38-54.

Dasgupta, R., Sen, J., & Mandal, N. (2021). Bending curvatures of subducting plates: old versus young slabs. Geophysical Journal International, 225(3), 1963-1981.

Dal Zilio, L., van Dinther, Y., Gerya, T. V., & Pranger, C. C. (2018). Seismic behaviour of mountain belts controlled by plate convergence rate. Earth and Planetary Science Letters, 482, 81-92.

Delph, J. R., Thomas, A. M., & Levander, A. (2021). Subcretionary tectonics: Linking variability in the expression of subduction along the Cascadia forearc. Earth and Planetary Science Letters, 556, 116724.

DeMets, C., Gordon, R. G., & Argus, D. F. (2010). Geologically current plate motions. Geophysical journal international, 181(1), 1-80.

DiPietro, J. (2018). Chapter 19 - Cascadia Volcanic Arc System, Geology and Landscape Evolution (Second Edition), Pages 473-499. ISBN 9780128111918. https://doi.org/10.1016/B978-0-12-811191-8.00019-1.

Eilon, Z. C., & Abers, G. A. (2017). High seismic attenuation at a mid-ocean ridge reveals the distribution of deep melt. Science advances, 3(5), e1602829.

Faccenda, M., & Capitanio, F. A. (2013). Seismic anisotropy around subduction zones: Insights from three-dimensional modeling of upper mantle deformation and SKS splitting calculations. Geochemistry, Geophysics, Geosystems, 14(1), 243-262.

Fan, J., & Zhao, D. (2021). Subslab heterogeneity and giant megathrust earthquakes. Nature Geoscience, 14(5), 349-353.

Gerya, T. (2019). Introduction to Numerical Geodynamic Modelling (2nd ed.). Cambridge: Cambridge University Press. doi:10.1017/9781316534243

Gerya, T. V., & Yuen, D. A. (2007). Robust characteristics method for modelling multiphase visco-elasto-plastic thermo-mechanical problems. Physics of the Earth and Planetary Interiors, 163(1-4), 83-105.

Heuret, A., Lallemand, S., Funiciello, F., Piromallo, C., & Faccenna, C. (2011). Physical characteristics of subduction interface type seismogenic zones revisited. Geochemistry, Geophysics, Geosystems, 12(1).

Honda, S., Morishige, M., & Orihashi, Y. (2007). Sinking hot anomaly trapped at the 410 km discontinuity near the Honshu subduction zone, Japan. Earth and Planetary Science Letters, 261(3-4), 565-577.

Jadamec, M. A., & Billen, M. I. (2010). Reconciling surface plate motions with rapid three-dimensional mantle flow around a slab edge. Nature, 465(7296), 338-341.

Kelsey, H. M., Engebretson, D. C., Mitchell, C. E., & Ticknor, R. L. (1994). Topographic form of the Coast Ranges of the Cascadia margin in relation to coastal uplift rates and plate subduction. Journal of Geophysical Research: Solid Earth, 99(B6), 12245-12255.

Krueger, H. E., & Wirth, E. A. (2017). Investigating segmentation in Cascadia: anisotropic crustal structure and mantle wedge serpentinization from receiver functions. Geochemistry, Geophysics, Geosystems, 18(10), 3592-3607.

Long, M. D. (2013). Constraints on subduction geodynamics from seismic anisotropy. Reviews of Geophysics, 51(1), 76-112.

Long, M. D. (2016). The Cascadia Paradox: Mantle flow and slab fragmentation in the Cascadia subduction system. Journal of Geodynamics, 102, 151-170.

Long, M. D., & Silver, P. G. (2009). Shear wave splitting and mantle anisotropy: Measurements, interpretations, and new directions. Surveys in Geophysics, 30(4), 407-461.

Martin-Short, R., Allen, R. M., Bastow, I. D., Totten, E., & Richards, M. A. (2015). Mantle flow geometry from ridge to trench beneath the Gorda–Juan de Fuca plate system. Nature Geoscience, 8(12), 965-968.

McCaffrey, R., Long, M. D., Goldfinger, C., Zwick, P. C., Nabelek, J. L., Johnson, C. K., & Smith, C. (2000). Rotation and plate locking at the southern Cascadia subduction zone. Geophysical Research Letters, 27(19), 3117-3120.

McCrory, P. A., Blair, J. L., Waldhauser, F., & Oppenheimer, D. H. (2012). Juan de Fuca slab geometry and its relation to Wadati-Benioff zone seismicity. Journal of Geophysical Research: Solid Earth, 117(B9).

Moresi, L., Dufour, F., & Mühlhaus, H. B. (2003). A Lagrangian integration point finite element method for large deformation modeling of viscoelastic geomaterials. Journal of computational physics, 184(2), 476-497.

Muldashev, I. A., & Sobolev, S. V. (2020). What controls maximum magnitudes of giant subduction earthquakes?. Geochemistry, Geophysics, Geosystems, 21(9), e2020GC009145.

Paczkowski, K., Montési, L. G., Long, M. D., & Thissen, C. J. (2014). Three-dimensional flow in the subslab mantle. Geochemistry, Geophysics, Geosystems, 15(10), 3989-4008.

Porritt, R. W., Allen, R. M., Boyarko, D. C., & Brudzinski, M. R. (2011). Investigation of Cascadia segmentation with ambient noise tomography. Earth and Planetary Science Letters, 309(1-2), 67-76.

Ranalli, G. (1995). Rheology of the Earth. Springer Science & Business Media.

Schellart, W. P., & Rawlinson, N. (2010). Convergent plate margin dynamics: New perspectives from structural geology, geophysics and geodynamic modelling. Tectonophysics, 483(1-2), 4-19.

Schmalzle, G. M., McCaffrey, R., & Creager, K. C. (2014). Central Cascadia subduction zone creep. Geochemistry, Geophysics, Geosystems, 15(4), 1515-1532.

Schmid, C., Goes, S., Van der Lee, S., & Giardini, D. (2002). Fate of the Cenozoic Farallon slab from a comparison of kinematic thermal modeling with tomographic images. Earth and Planetary Science Letters, 204(1-2), 17-32.

Stüwe, Kurt. Geodynamics of the Lithosphere. Springer, 2007.

Toomey, D. R., Allen, R. M., Barclay, A. H., Bell, S. W., Bromirski, P. D., Carlson, R. L., ... & Wilcock, W. S. (2014). The Cascadia Initiative: A sea change in seismological studies of subduction zones. Oceanography, 27(2), 138-150.

Turcotte, D. L., & Schubert, G. (2012). Geodynamics. Cambridge university press.

van Dinther, Y., Morra, G., Funiciello, F., & Faccenna, C. (2010). Role of the overriding plate in the subduction process: Insights from numerical models. Tectonophysics, 484(1-4), 74-86.

Van Dinther, Y., Gerya, T. V., Dalguer, L. A., Mai, P. M., Morra, G., & Giardini, D. (2013). The seismic cycle at subduction thrusts: Insights from seismo-thermo-mechanical models. Journal of Geophysical Research: Solid Earth, 118(12), 6183-6202.

van Dinther, Y., Gerya, T. V., Dalguer, L. A., Corbi, F., Funiciello, F., & Mai, P. M. (2013). The seismic cycle at subduction thrusts: 2. Dynamic implications of geodynamic simulations validated with laboratory models. Journal of Geophysical Research: Solid Earth, 118(4), 1502-1525.

van Dinther, Y., Mai, P. M., Dalguer, L. A., & Gerya, T. V. (2014). Modeling the seismic cycle in subduction zones: The role and spatiotemporal occurrence of off-megathrust earthquakes. Geophysical Research Letters, 41(4), 1194-1201.

Venereau, C. M. A., Martin-Short, R., Bastow, I. D., Allen, R. M., & Kounoudis, R. (2019). The role of variable slab dip in driving mantle flow at the eastern edge of the Alaskan subduction margin: Insights from shear-wave splitting. Geochemistry, Geophysics, Geosystems, 20(5), 2433-2448.

Wilson, D. S., Kirby, S., Wang, K., & Dunlop, S. (2002). The Juan de Fuca plate and slab: Isochron structure and Cenozoic plate motions. The Cascadia subduction zone and related subduction systems, 4350, 9-12.

Long, M. D., & Wirth, E. A. (2013). Mantle flow in subduction systems: The mantle wedge flow field and implications for wedge processes. Journal of Geophysical Research: Solid Earth, 118(2), 583-606.

Zhao, D., & Hua, Y. (2021). Anisotropic tomography of the Cascadia subduction zone. Physics of the Earth and Planetary Interiors, 318, 106767.

Appendix

Depth of the anomaly

The depth of the anomaly described here is the depth of its center from the top of the model (top of the thick air layer).

a. Slab dip

The models do not predict any significant change for different initial depths of the anomaly (Figure 15).

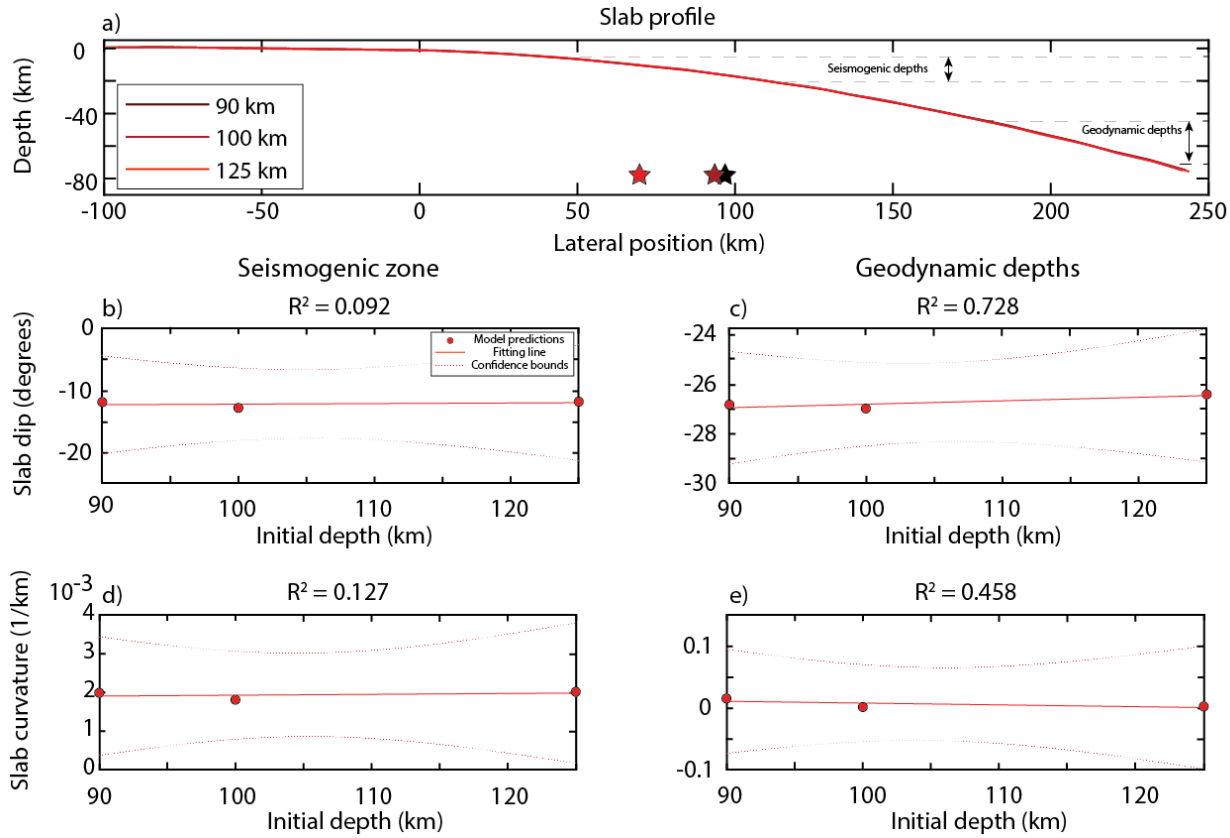

Figure 16: Slab profiles (a), slab dip (b-c) and apparent slab curvature (d-e) for different initial depth of a density anomaly with an effective density contrast of 4.1 kg/m^3 at t = 7.9 Myrs. (a) Stars indicate the horizontal center of the anomaly at the last timestep. The dashed lines delimit the seismogenic zone and the geodynamic depths areas of calculation of the slab dip and the slab curvature. (b-c) Seismogenic zone (b) and geodynamic depths (c). The less negative the value is, the shallower the slab dip is. (d-e) Seismogenic zone (d) and geodynamic depths (e). (b-e) The red dots are the model results, while the red lines are the linear regressions that fit the predictions best estimated using a root-mean-square (RMS) error method where R^2 = 1 is the best fit, the dashed lines are the 95% confidence bounds of the regression line. Slab curvature is calculated using circfit (Andrew Horchler (2022). Circfit (https://github.com/horchler/circfit), GitHub. Retrieved June 8, 2022) to extract the bending radius of the slab and obtain the slab curvature from 1/R where R is the bending radius (Turcotte and Schubert, 2012).

b. Topography

Results are inconsistent, no clear trend can be observed here.

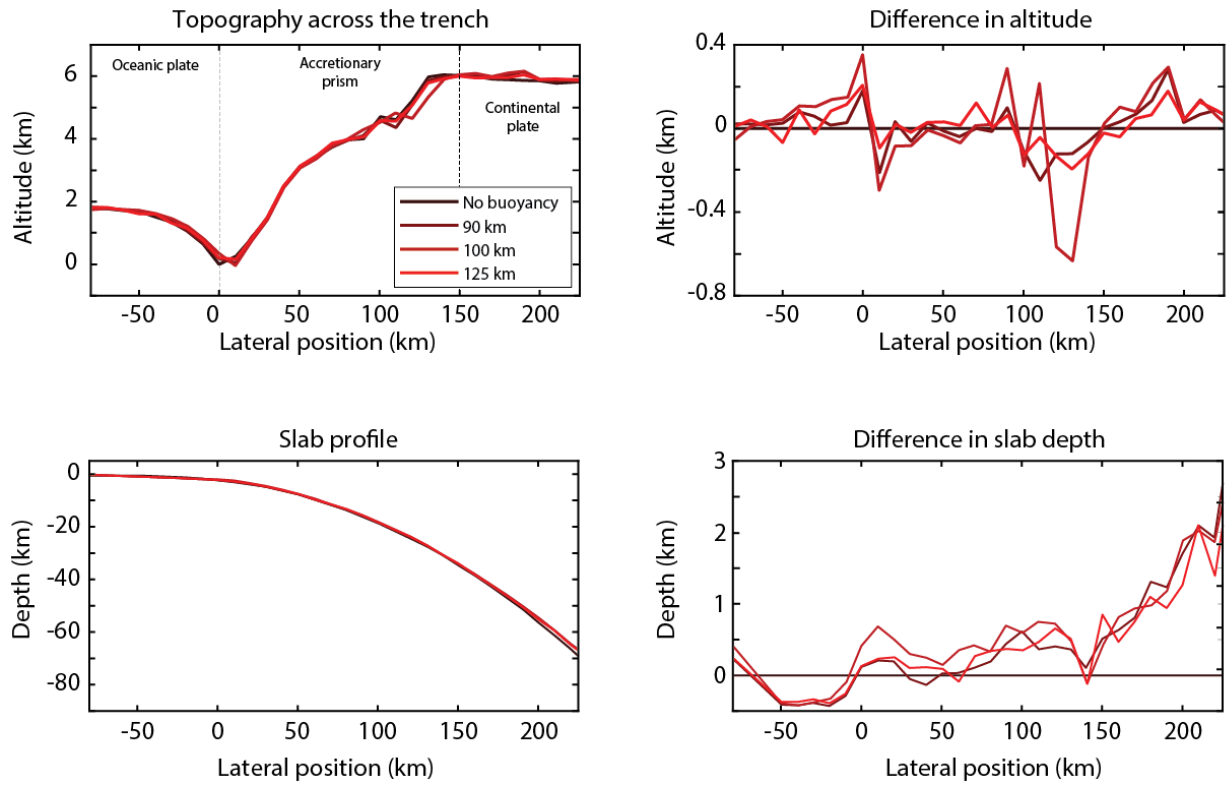

Figure 17: Topography (a-b) and slab profiles (c-d) for varying initial depths of the sub-slab density anomaly from the left boundary for an effective density contrast of 4.1 kg/m^3 at t = 7.9 Myrs. (a) Altitude with respect to the trench at the isostatic equilibrium for varying density contrasts. Dashed lines are the limits between the oceanic plate and the accretionary prism, and the accretionary prism and the continental plate. (b) Changes in topography. (c) Slab profiles for varying density contrasts corrected for isostatic equilibrium to have an initial depth of 0 for all models. (d) Variations in vertical position of the slab with respect the reference model without buoyancy.

c. Earthquake sequences

Interseismic coupling

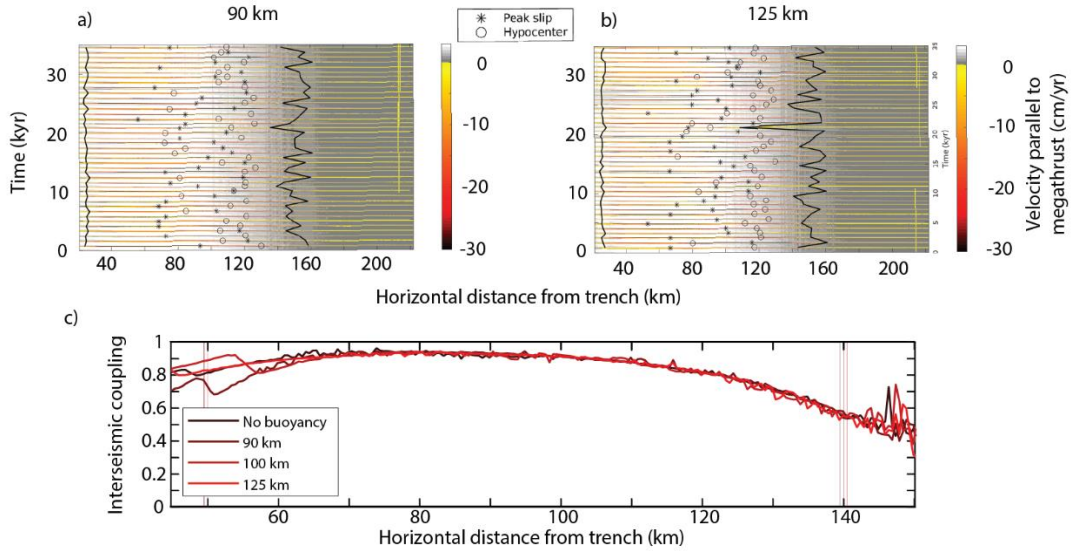

Figure 18: Velocity parallel to the megathrust (a-b) and interseismic coupling (c). (a-b) Velocity parallel 6.4 km above the megathrust (overriding plate) for the reference model (a) and 4.1 kg/m^3 of effective density contrasts (b). Velocities are positive (gray-white) towards the continent. Continuous black lines are the limits of the ruptures for each event. Circles are hypocenter locations and starts are the peak slip locations. (c) Interseismic coupling for different density contrasts. Calculated by the ratio of velocities at 6.4 km above and below the megathrust, 1 is the theoretical value for two fully coupled plates. The vertical lines are the up- and downdip limits of the seismogenic zone based on the 150 and 350°C isotherms.

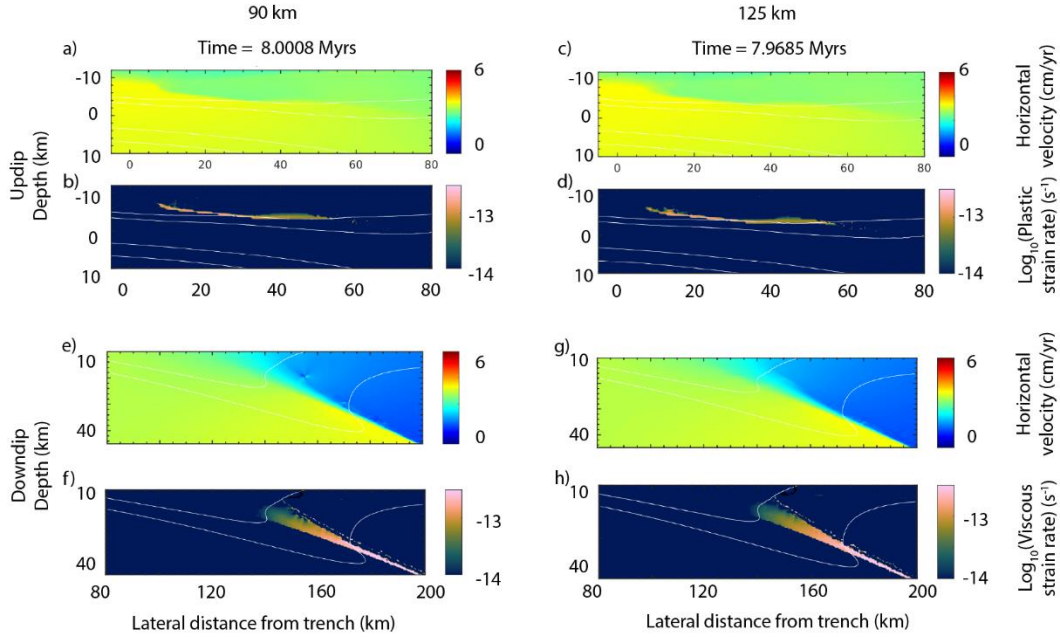

Figure 12: Visco-plastic strain rates at the megathrust for different initial depths of the sub-slab buoyant anomaly with an effective density contrast of 4.1 kg/m^3. (a-d) Snapshot of horizontal velocity (a-b) and plastic strain rate (lower c-d) in the updip region. The plastic strain rates are displayed in a log scale. The white lines indicate the 100°C, 150°C, 350°C, and 450°C isotherms. (e-h) Snapshot of horizontal velocity (e-f panel) and plastic strain rate (g-h) in the downdip region. The white lines indicate the 350°C and 450°C isotherms. (a, c, e, g) 90 km. (b, d, f, h) 125 km.

Rupture widths

Varying the initial depth of the anomaly does not seem to significantly affect the seismicity.

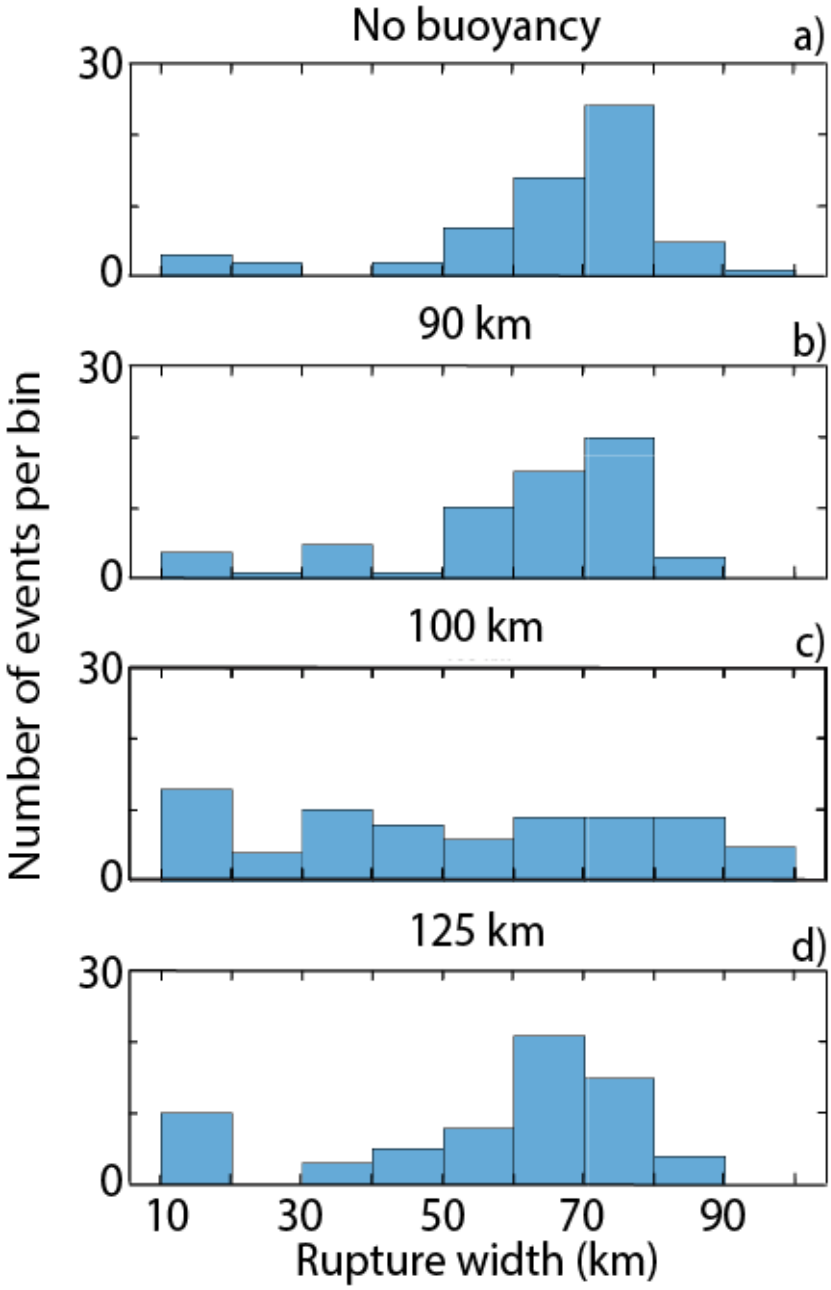

Figure 19: Rupture width distribution for varying anomaly initial depths. Panels are ordered from the oldest slab (top) to the youngest slab (bottom). The x-axis represents the rupture width of the events binned into 10-km bins and the y-axis is the density of events per bin.